

Fracture of solar-grade anisotropic polycrystalline Silicon: A combined phase field–cohesive zone model approach

M. Paggi^{a,*}, M. Corrado^b, J. Reinoso^c

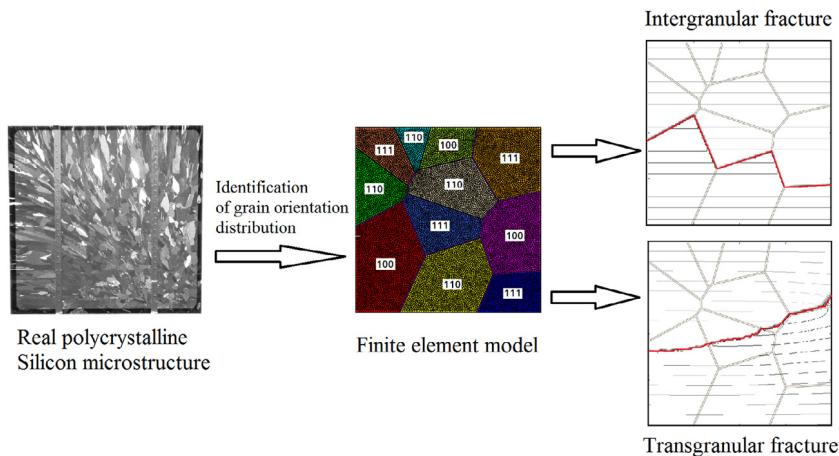
^a *IMT School for Advanced Studies Lucca, Piazza San Francesco 19, 55100 Lucca, Italy*

^b *Department of Structural, Geotechnical and Building Engineering, Politecnico di Torino, Corso Duca degli Abruzzi 24, 10129, Torino, Italy*

^c *Elasticity and Strength of Materials Group, School of Engineering, Universidad de Sevilla, Camino de los Descubrimientos s/n, 41092 Sevilla, Spain*

Received 26 May 2017; received in revised form 19 October 2017; accepted 20 October 2017

Graphical Abstract



Highlights

- Combined phase-field and cohesive zone model for fracture.
- Transgranular and intergranular fracture in solar-grade Silicon.
- Anisotropic phase field model for fracture.
- Identification of polycrystalline Silicon mechanical parameters.

* Corresponding author.

E-mail address: marco.paggi@imtlucca.it (M. Paggi).

<https://doi.org/10.1016/j.cma.2017.10.021>

0045-7825/© 2017 The Author(s). Published by Elsevier B.V. This is an open access article under the CC BY-NC-ND license (<http://creativecommons.org/licenses/by-nc-nd/4.0/>).

Abstract

This work presents a novel computational framework to simulate fracture events in brittle anisotropic polycrystalline materials at the microscopical level, with application to solar-grade polycrystalline Silicon. Quasi-static failure is modeled by combining the phase field approach of brittle fracture (for transgranular fracture) with the cohesive zone model for the grain boundaries (for intergranular fracture) through the generalization of the recent FE-based technique published in [M. Paggi, J. Reinoso, *Comput. Methods Appl. Mech. Engrg.*, 31 (2017) 145–172] to deal with anisotropic polycrystalline microstructures. The proposed model, which accounts for any anisotropic constitutive tensor for the grains depending on their preferential orientation, as well as an orientation-dependent fracture toughness, allows to simulate intergranular and transgranular crack growths in an efficient manner, with or without initial defects. One of the advantages of the current variational method is the fact that complex crack patterns in such materials are triggered without any user-intervention, being possible to account for the competition between both dissipative phenomena. In addition, further aspects with regard to the model parameters identification are discussed in reference to solar cells images obtained from transmitted light source. A series of representative numerical simulations is carried out to highlight the interplay between the different types of fracture occurring in solar-grade polycrystalline Silicon, and to assess the role of anisotropy on the crack path and on the apparent tensile strength of the material.

© 2017 The Author(s). Published by Elsevier B.V. This is an open access article under the CC BY-NC-ND license (<http://creativecommons.org/licenses/by-nc-nd/4.0/>).

Keywords: Cohesive zone model; Phase field modeling of fracture; Anisotropic elasticity; Solar-grade polycrystalline silicon; Finite element method

1. Introduction

Accurate prediction of failure in solids is a matter of a great relevance in different industrial sectors ranging from aerospace and aeronautics to renewable energy. At the macroscopic scale, fracture is generally originated by several microscopic defects, i.e. voids and cracks, which grow and coalesce leading to the deterioration of the overall material properties and the load carrying capacity of the structural component. In particular, at the microscopical scale, the interplay between intergranular (cracks propagating along grain boundaries) and transgranular (cracks propagating through the grains) fracture in polycrystalline materials is of major concern in material science and engineering applications.

In the related literature, simplified models specific for intergranular fracture have been proposed in [1–5] based on the cohesive zone model (CZM) inserted along the internal grain boundaries. Cohesive crack formulations can be understood as phenomenological models in which fracture events are triggered by evaluating a particular traction–displacement law. This numerical technique inherently incorporates a characteristic length scale and has been widely used to simulate damage in polycrystalline materials [6], though crack paths are constrained along element edges, see a wide discussion in [7–9], among others.

However, transgranular fracture is also a relevant failure mode in some materials and, in many cases, it is developed in competition with intergranular failure. Therefore, the development of numerical techniques that allow a reliable modeling of grains cracking with arbitrary failure paths are indeed necessary to provide a comprehensive simulation tool. In practical situations, for instance in micro-electro-mechanical systems (MEMS), both types of crack propagation have been reported in [10,11]. In those investigations, the authors comprehensively document the importance of considering the in plane grain anisotropy of Silicon which notably affects the fracture behavior. More specifically, regarding photovoltaics systems, solar-grade polycrystalline Silicon with grains randomly oriented in 3D are frequently used to manufacture thin solar cells. In such a case, both intergranular and transgranular fracture have been experimentally reported [12,13], see also some crack patterns in Fig. 1 experimentally observed by the present authors in solar cells embedded in photovoltaic modules, using the electroluminescence technique. A first attempt to model both types of fracture has been pursued in [14] by an intrinsic cohesive zone model approach. To avoid mesh dependency and un-physical material compliances, the extrinsic approach could be put forward, as in [15]. However, for very brittle materials like Silicon, cohesive zone model approaches suffer from the complexity in resolving the process zone which is very small as compared to the grain size or to the specimen size.

In contrast to the previous numerical methods relying on cohesive zone models only, several studies have also been proposed to account for transgranular crack propagation in polycrystals by means of the extended finite element

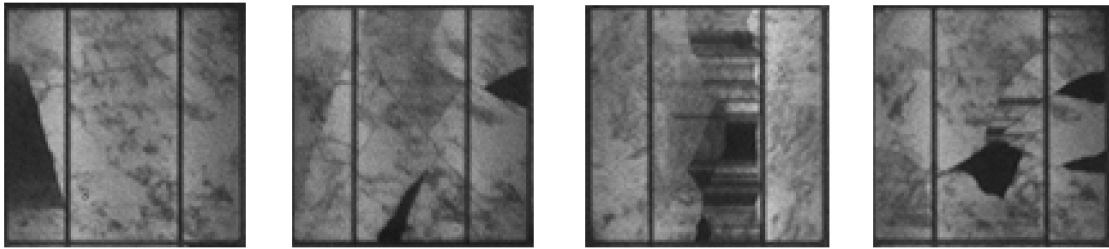


Fig. 1. Examples of crack patterns in polycrystalline Silicon solar cells embedded in photovoltaic modules. Dark areas in the images correspond to electrically inactive zones not contributing to energy production.

method (X-FEM) [16], whereby the crack path does not explicitly depend upon the underlying spatial discretization of the physical domain into finite elements. In particular, Sukumar and co-authors [17] advocated a failure criterion based on the ratio between the fracture toughness of the grain boundaries \mathcal{G}_c^{gb} and the toughness of the grains \mathcal{G}_c^i , achieving a good qualitative agreement with respect to the experimental observations therein analyzed. Alternative computational techniques that feature explicit crack representations such as the enhanced finite element method (EFEM) [18,19], relying on the enhanced assumed variational methods [20], and the generalized finite element method (GFEM) [21] can also be used to model fracture events in such scenarios, though different operative difficulties such as the identification of crack initiation location and path might arise.

Within the context of modeling sharp crack discontinuities, the recent phase field approaches for fracture [22,23] can be seen as a very promising numerical technique, especially suitable for quasi-brittle materials like Silicon (monocrystalline and polycrystalline solar-grade). Particularly, the explicit crack methods as those mentioned above suffer in situations with very complex fracture topologies including branching, kinking and coalescence. With the aim of overcoming such difficulties, grounded on the Griffith's fracture theory [24], phase field models encompass a diffusive crack approach based on the definition of the crack phase field variable and its corresponding evolution equation. In the spirit of the Γ -convergence regularizations [25,26], discontinuities due to cracks are regularized using a characteristic length scale l . One of the most appealing aspects of phase field models of fracture is their inherent versatility, sharing several common aspects with gradient-enhanced damage formulations [27–30]. This feature has motivated the extension of the thermodynamic consistent formulation proposed by Miehe and co-authors [22,31] to dynamic [32,23] and ductile [33] fracture, anisotropic fracture in biomechanics [34], multi-physic systems [35,36], and shell structures [37–40], among many others. In this concern, recent investigations have applied the phase field approach to simulate failure in polycrystalline materials [41–43]. Moreover, its rational coupling with a novel cohesive formulation proposed in [44] allows fundamental Linear Elastic Fracture Mechanics (LEFM) predictions to be retrieved for the limit case of brittle cohesive interfaces in a consistent and robust manner. This formulation conceptually postulated the split of the dissipated energy into the bulk and interface contributions for the interplay between both failure mechanisms, i.e. crack growth in the bulk or debonding along the existing interfaces.

Departing from the computational framework developed in [44], a novel formulation based on the phase field modeling of fracture for the grains combined with the cohesive zone model for the grain boundaries is proposed in this article. The principal motivation for the combination of both the cohesive zone and phase field models for triggering damage events in polycrystalline materials is to capture the fracture phenomena related to intergranular and transgranular crack growth and their potential interplay. Polycrystalline Silicon grains for solar-grade photovoltaics display a very brittle response, so that the use of the phase field approach to brittle fracture, herein extended to anisotropic materials with elastic and toughness properties dependent on the grain orientation, is a proper choice. Regarding the grain boundaries, on the other hand, a cohesive zone model approach is pursued to simulate their separation and allow for a richer description of their fracture behavior. In fact, although a tension cut-off cohesive zone model will be used in the present study, interface finite elements used to discretize the grain boundaries can accommodate more accurate traction–separation relations stemming from molecular dynamics or ab initio simulations, see e.g. [45,46], towards the development of a multi-scale computational model of technological impact for photovoltaic applications. Moreover, the proposed interface finite element formulation can be extended to take into account the additional thermal resistance of the grain boundaries for multi-field problems, which in turn does depend on the crack opening at the sub-micro scale, following the approach put forward in [47]. Within such a framework,

further developments might also regard modeling of the optoelectronic properties of grain boundaries [48], which is an important concern for the solar energy conversion efficiency.

Based on the previous considerations, the main goal of the current approach concerns the simulation of fracture events in anisotropic polycrystalline materials with high technological impact, as is the case of solar-grade polycrystalline Silicon. First, the proposed formulation extends the concepts introduced in [44] for anisotropic materials via the definition of the fracture toughness of the grains as a function of the grain orientation. This modification will be used in the unified variational principle for the competition between intergranular and transgranular crack propagation. Second, due to the practical importance of polycrystalline Silicon in solar systems, special attention is devoted for identification of the model parameters for such applications through the use of solar cells images from transmitted light source.

The manuscript is organized as follows. In Section 2, the principal aspects of the proposed modeling framework to simulate intergranular and transgranular failure in polycrystalline microstructures are presented, where special attention is paid to the modeling assumptions of anisotropic behavior of solar-grade Silicon. Section 3 outlines the determination of the actual material properties of solar cells obtained from Silicon wafers in solar energy systems. Algorithmic details regarding the insertion of interface models within the grain boundaries are addressed in Section 4. The performance of the proposed computational method is assessed in Section 5 by means of several representative examples. Finally, the main conclusions of the present study are drawn in Section 6. Additional electronic material collects MATLAB routines for the generation of finite element meshes for polycrystalline materials and for the computation of the anisotropic constitutive tensor of the solar-grade Silicon grains depending on their orientation, adopting the conventional Miller indices representation used in materials science.

2. Phase field approach for transgranular crack growth combined with the cohesive zone model for intergranular fracture

This section revisits the main aspects of the consistent modeling framework for the combination of the phase field approach of fracture for transgranular crack growth and the cohesive zone model used to simulate intergranular fracture. Section 2.1 outlines the variational framework and the interface model, whereas the corresponding weak form and finite element formulation is presented in Section 2.2. Subsequently, Section 2.3 addresses the main aspects concerning the material modeling for anisotropic Silicon grains. As stated above, from the computational standpoint, the main novelty of the current study concerns the incorporation of the anisotropic character of polycrystalline materials –particularized to Silicon photovoltaics– in terms of elastic and fracture properties within the original modeling framework proposed in [44]. Therefore, this technique allows for the simulation of the competition between intergranular and transgranular crack propagation in an efficient and robust manner.

2.1. Variational framework and interface formulation

Let $\Omega \in \mathbb{R}^{n_{dim}}$ be an arbitrary cracked solid in the Euclidean space of dimension n_{dim} , whose boundary is denoted by $\partial\Omega$. Let $\Gamma \in \mathbb{R}^{n_{dim}-1}$ the crack surface within Ω , see Fig. 2.a. This system also includes the presence of an interface Γ_i . To clarify the notation, in the sequel, the position vectors of the grains are denoted by \mathbf{x} , whereas \mathbf{x}_c stands for the position vectors referred to the interface Γ_i .

The variational approach to brittle fracture governing crack nucleation, propagation and branching is set up through the definition of the following functional [22,23]:

$$\Pi(\mathbf{u}, \Gamma) = \Pi_{\Omega}(\mathbf{u}, \Gamma) + \Pi_{\Gamma}(\Gamma) = \int_{\Omega \setminus \Gamma} \psi^e(\boldsymbol{\varepsilon}) d\Omega + \int_{\Gamma} \mathcal{G}_c d\Gamma, \quad (1)$$

where $\psi^e(\boldsymbol{\varepsilon})$ is the elastic energy density that depends upon the strain field $\boldsymbol{\varepsilon}$, and \mathcal{G}_c is the fracture energy. In Eq. (1), the term $\Pi_{\Omega}(\mathbf{u}, \Gamma)$ identifies the elastic energy stored in the damaged body, while the energy required to create the crack complying with the Griffith criterion is denoted by $\Pi_{\Gamma}(\Gamma)$.

Following [44,49], the fracture energy function is split into the corresponding counterparts associated with the dissipated energy in the anisotropic polycrystalline grains Ω due to transgranular fracture (governed by the phase field approach of brittle fracture for the prospective discontinuities Γ_t) and along the grain boundaries (Γ_i) as a manifestation of intergranular fracture:

$$\Pi_{\Gamma} = \Pi_{\Gamma_t} + \Pi_{\Gamma_i} = \int_{\Gamma_t} \mathcal{G}^{(abc)}(\mathbf{u}, \vartheta) d\Gamma + \int_{\Gamma_i} \mathcal{G}^i(\mathbf{u}, \vartheta) d\Gamma. \quad (2)$$

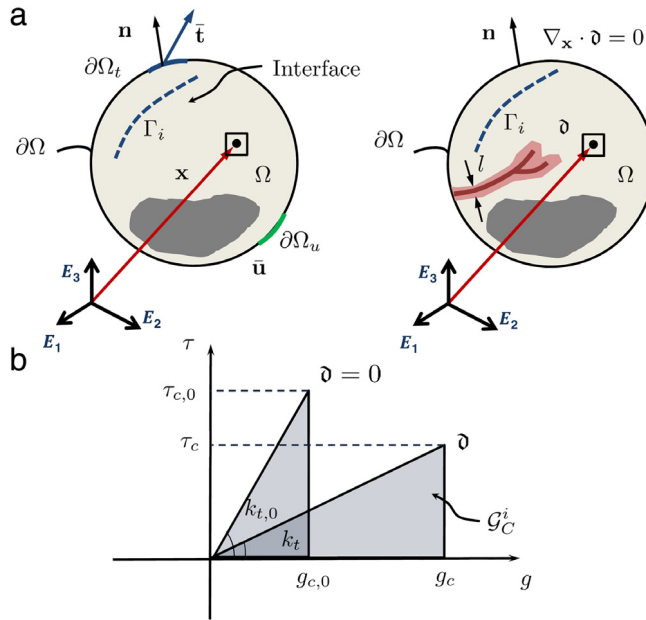


Fig. 2. (a) The multi-field problem for cracked bodies based on the phase field approach of fracture with the presence of interfaces Γ_i . Left: Mechanical problem. Right: Crack phase field problem. (b) Traction–separation law of the interface model compatible with the phase field approach of fracture: representation for a generic fracture Mode that releases the energy \mathcal{G}_C^i : τ , $\tau_{c,0}$ and τ_c are the traction component at the interface, its critical value for undamaged and partially damaged surrounding bulk, whilst g , $g_{c,0}$ and g_c are their respective relative displacements at the interface.

In the grains, the fracture energy is dissipated according to the Griffith hypothesis [50]. In the present anisotropic model, the fracture toughness of each grain, $\mathcal{G}^{(abc)}$, depends on the grain orientation $\langle abc \rangle$, where a , b , and c denote the standard Miller indices.

The phase field variable in Eq. (2) has the physical meaning of an internal state damage variable ($\vartheta \in [0, 1]$, where $\vartheta = 0$ represents an intact material, while $\vartheta = 1$ identifies the fully damaged state), which is an implicit function of the displacement field and of a regularization parameter related to the smeared crack width, l . When the characteristic regularization parameter tends to zero ($l \rightarrow 0$), then the formulation outlined in Eq. (2) tends to Eq. (1) in the sense of the so-called Γ -convergence (see [50] for more details). For finite non-vanishing values of l , this parameter controls the value of the apparent material strength in uniaxial tensile tests, see e.g. [44]. At this point, it is worth mentioning that recent studies have investigated the relation between the parameter l and the failure stress $\sigma_c = \sqrt{\mathcal{G}_c^b E/L}$, where L is the characteristic size of the specimen and \mathcal{G}_c^b and E stand for the toughness and the Young’s modulus of the bulk, respectively. In particular, Tanné and co-authors [51] proposed that, once these material properties are known, i.e. σ_c , \mathcal{G}_c^b and E , then the parameter l can be set as $l = \frac{27}{256} \left(\frac{\mathcal{G}_c^b E}{\sigma_c^2} \right)$. Therefore, based on this consideration, the regularization parameter can be considered as a material internal length scale, in line with the discussion in [52,53].

For the grain boundaries, the corresponding fracture energy is released according to a cohesive zone model formulation. In particular, in the following we assume that the interface behavior is ruled by a linear traction–separation relation with tension cut-off, to simulate the brittle response of solar-grade polycrystalline Silicon. According to [44], the energy dissipation for intergranular fracture is characterized by the fracture energy function \mathcal{G}^i , which is related to the displacement discontinuities at the interface, \mathbf{g} , and also to the average phase field degradation variable of the adjacent continuum, ϑ :

$$\mathcal{G}^i = \mathcal{G}(\mathbf{g}, \vartheta). \tag{3}$$

In the present study, a linear tension cut-off cohesive zone model (CZM) is adopted for Mode I and Mode II interface fracture, see [44] for more details omitted here for the sake of conciseness. The traction–separation relations are defined by the peak tractions σ_{\max} and τ_{\max} , and by the areas below them, which respectively correspond to the

grain boundary Mode I and Mode II fracture toughnesses, see Fig. 2.b for a schematic representation of the interface response.

The particular forms of the traction–separation relation of the current cohesive model, which depends on the damage state of the surrounding bulk relying on the phase field variable, are given by:

$$\sigma = \begin{cases} k_n \frac{g_n}{g_{nc}}, & \text{if } 0 < \frac{g_n}{g_{nc}} < 1; \\ 0, & \text{if } \frac{g_n}{g_{nc}} \geq 1, \end{cases} \quad \tau = \begin{cases} k_t \frac{g_t}{g_{tc}}, & \text{if } 0 < \frac{g_t}{g_{tc}} < 1; \\ 0, & \text{if } \frac{g_t}{g_{tc}} \geq 1. \end{cases} \quad (4)$$

It is worth mentioning that, differing from [43], the shape of the proposed cohesive model is consistently coupled with the phase field model in the bulk, but preserving the energy dissipated along the interface. The corresponding energy release rates for Modes I and II read:

$$\mathcal{G}_I^i(\vartheta) = \frac{1}{2} k_{n,0} g_n^2 \frac{g_{nc,0}^2}{[(1 - \vartheta)g_{nc,0} + \vartheta g_{nc,1}]^2}; \quad \mathcal{G}_{II}^i(\vartheta) = \frac{1}{2} k_{t,0} g_t^2 \frac{g_{tc,0}^2}{[(1 - \vartheta)g_{tc,0} + \vartheta g_{tc,1}]^2}, \quad (5)$$

where $k_{n,0}$ and $k_{t,0}$ stand for the interface stiffness values for $\vartheta = 0$, with their corresponding critical relative displacements $g_{nc,0}$ and $g_{tc,0}$. The respective values for $\vartheta = 1$ are denoted by $k_{n,1}$, $k_{t,1}$, $g_{nc,1}$ and $g_{tc,1}$. Finally, for a generic value of the crack phase field variable in the bulk, ϑ , the corresponding interface parameters read: k_n , k_t , g_{nc} and g_{tc} , whose definitions can be found in [44].

Interface failure is attained through the adoption of the standard fracture criterion based on the quadratic composition of the Mode I and Mode II energy release rates:

$$\left(\frac{\mathcal{G}_I^i}{\mathcal{G}_{IC}^i}\right)^2 + \left(\frac{\mathcal{G}_{II}^i}{\mathcal{G}_{IIC}^i}\right)^2 = 1. \quad (6)$$

Based on the previous modeling assumptions, the functional in Eq. (1) can be recast as:

$$\Pi(\mathbf{u}, \Gamma_t, \Gamma_i) = \Pi_\Omega + \Pi_{\Gamma_t} + \Pi_{\Gamma_i} = \int_{\Omega \setminus \Gamma} \psi^e(\boldsymbol{\varepsilon}) \, d\Omega + \int_{\Gamma_t} \mathcal{G}^{(abc)}(\mathbf{u}, \vartheta) \, d\Gamma + \int_{\Gamma_i} \mathcal{G}^i(\mathbf{g}, \mathfrak{h}, \vartheta) \, d\Gamma, \quad (7)$$

where the functional corresponding to the grains is:

$$\Pi_t(\mathbf{u}, \Gamma_t) = \Pi_\Omega(\mathbf{u}, \Gamma_t) + \Pi_{\Gamma_t}(\Gamma_t) = \int_{\Omega \setminus \Gamma} \psi^e(\boldsymbol{\varepsilon}) \, d\Omega + \int_{\Gamma_t} \mathcal{G}^{(abc)}(\mathbf{u}, \vartheta) \, d\Gamma. \quad (8)$$

Within the regularized framework of the phase field approach in continuous bodies [54], given a crack surface topology $\Gamma_c \subset \mathbb{R}^2$, the regularized crack functional adopts the form

$$\Gamma_c(\vartheta) := \int_{\Omega} \gamma(\vartheta, \nabla_x \vartheta) \, d\Omega, \quad \text{with} \quad \gamma(\vartheta, \nabla_x \vartheta) = \frac{1}{2l} \vartheta^2 + \frac{l}{2} |\nabla_x \vartheta|^2. \quad (9)$$

In line with [22,31], the minimization problem associated with the diffusive crack topology reads

$$\vartheta(\mathbf{x}) = \text{Arg}\left\{ \inf_{\vartheta \in \mathcal{W}_{\Gamma_c(t)}} \Gamma_c(\vartheta) \right\} \quad (10)$$

subject to the Dirichlet-type constraint: $\mathcal{W}_{\Gamma_c(t)} = \{\vartheta \mid \vartheta(\mathbf{x}) = 1 \text{ at } \mathbf{x} \in \Gamma_c\}$. Correspondingly, the potential energy of the system is decomposed into two terms:

$$\Pi_t(\mathbf{u}, \vartheta) = \int_{\Omega} \psi(\boldsymbol{\varepsilon}, \vartheta) \, d\Omega + \int_{\Omega} \mathcal{G}^{(abc)} \gamma(\vartheta, \nabla_x \vartheta) \, d\Omega. \quad (11)$$

As a result, the total free energy density of the bulk, $\hat{\psi}$, reads:

$$\hat{\psi}(\boldsymbol{\varepsilon}, \vartheta) = \psi(\boldsymbol{\varepsilon}, \vartheta) + \mathcal{G}^{(abc)} \gamma(\vartheta, \nabla_x \vartheta). \quad (12)$$

The corresponding Euler equations associated with the phase field problem within the grains are given by

$$\vartheta - l^2 \nabla_x^2 \vartheta = 0 \text{ in } \Omega \quad \text{and} \quad \nabla_x \vartheta \cdot \mathbf{n} = 0 \text{ in } \partial\Omega, \quad (13)$$

where $\nabla_x^2 \vartheta$ stands for the Laplacian of the phase field variable.

Regarding the strain energy density of the bulk, $\psi(\boldsymbol{\epsilon}, \vartheta)$, the following expression is herein considered, accounting for the anisotropic constitutive response of the grains:

$$\psi(\boldsymbol{\epsilon}, \vartheta) = \mathfrak{g}(\vartheta)\psi^e(\boldsymbol{\epsilon}) = [(1 - \vartheta)^2 + \mathcal{K}] \psi^e(\boldsymbol{\epsilon}). \tag{14}$$

In the previous equation, $\psi^e(\boldsymbol{\epsilon})$ is the elastic strain energy density of each undamaged anisotropic grain under plane stress assumptions, whereas $\mathfrak{g}(\vartheta)$ stands for the degradation function, which satisfies $\mathfrak{g}(0)\psi^e(\boldsymbol{\epsilon}) = \psi^e(\boldsymbol{\epsilon})$ for undamaged states, and $\mathfrak{g}(1)\psi^e(\boldsymbol{\epsilon}) = \mathcal{K}\psi^e(\boldsymbol{\epsilon})$ for fully deteriorated states, being \mathcal{K} a residual positive parameter that prevents numerical instabilities.

Hence, the resulting form of the functional corresponding to the current modeling framework reads

$$\Pi(\mathbf{u}, \vartheta) = \int_{\Omega} \mathfrak{g}(\vartheta)\psi^e(\boldsymbol{\epsilon}) \, d\Omega + \int_{\Omega} \mathcal{G}^{(abc)}\gamma(\vartheta, \nabla_{\mathbf{x}}\vartheta) \, d\Omega + \int_{\Gamma_i} \mathcal{G}^i(\mathbf{g}, \vartheta) \, d\Gamma. \tag{15}$$

Finally, note also that a suitable decomposition of the free-energy function into positive and negative counterparts as proposed in [22] is recalled to preclude crack propagation under compression.

2.2. Weak form of the variational problem and finite element formulation

The construction of the variational formulation is carried out through the exploitation of the variation of the functional given in Eq. (15) with respect to the displacements and the crack phase field variable.

For transgranular failure, we postulate kinematic and traction boundary conditions, which are defined along the disjoint parts $\partial\Omega_u \subset \partial\Omega$ and $\partial\Omega_t \subset \partial\Omega$, respectively, with $\partial\Omega_t \cup \partial\Omega_u = \partial\Omega$ and $\partial\Omega_t \cap \partial\Omega_u = \emptyset$, yielding:

$$\mathbf{u} = \bar{\mathbf{u}} \quad \text{on } \partial\Omega_u \quad \text{and} \quad \bar{\mathbf{t}} = \boldsymbol{\sigma} \cdot \mathbf{n} \quad \text{on } \partial\Omega_t, \tag{16}$$

where \mathbf{n} is the outward normal unit vector to the body, and $\boldsymbol{\sigma}$ is the Cauchy stress tensor.

Recalling standard arguments, the following weak form for the variational problem for the grains is obtained:

$$\begin{aligned} \delta\Pi_t(\mathbf{u}, \delta\mathbf{u}, \vartheta, \delta\vartheta) &= \int_{\Omega} \boldsymbol{\sigma} : \delta\boldsymbol{\epsilon} \, d\Omega - \int_{\Omega} 2(1 - \vartheta)\delta\vartheta\psi^e(\boldsymbol{\epsilon}) \, d\Omega \\ &\quad + \int_{\Omega} \mathcal{G}^{(abc)}l \left[\frac{1}{l^2}\vartheta\delta\vartheta + \nabla_{\mathbf{x}}\vartheta \cdot \nabla_{\mathbf{x}}(\delta\vartheta) \right] \, d\Omega + \delta\Pi_{t,\text{ext}}(\mathbf{u}, \delta\mathbf{u}), \end{aligned} \tag{17}$$

where $\delta\mathbf{u}$ collects the test functions referred to the displacement field, which satisfy ($\mathfrak{V}^u = \{\delta\mathbf{u} \mid \mathbf{u} = \bar{\mathbf{u}} \text{ on } \partial\Omega_u, \mathbf{u} \in \mathcal{H}^1\}$); $\delta\vartheta$ identifies the phase field test functions ($\mathfrak{V}^\vartheta = \{\delta\vartheta \mid \delta\vartheta = 0 \text{ on } \Gamma_b, \vartheta \in \mathcal{H}^0\}$), and finally, the external contribution to the variation of the bulk functional reads

$$\delta\Pi_{t,\text{ext}}(\mathbf{u}, \delta\mathbf{u}) = \int_{\partial\Omega} \bar{\mathbf{t}} \cdot \delta\mathbf{u} \, d\partial\Omega + \int_{\Omega} \mathbf{f}_v \cdot \delta\mathbf{u} \, d\Omega. \tag{18}$$

The irreversible character of the fracture process within the grains is guaranteed by means of the incorporation of a penalty term accounting for the history of the local damage variable [22,55]. The thermodynamic consistency according to the Clausius–Planck inequality of the present formulation has been comprehensively addressed in [22], and consequently specific details are omitted here for the sake of brevity.

Similarly, with regard to the interface contribution to the complete functional of the system, its virtual variation with respect to the two primary fields takes the form

$$\delta\Pi_{\Gamma_i}(\mathbf{u}, \delta\mathbf{u}, \vartheta, \delta\vartheta) = \int_{\Gamma_i} \left(\frac{\partial\mathcal{G}^i(\mathbf{u}, \vartheta)}{\partial\mathbf{u}}\delta\mathbf{u} + \frac{\partial\mathcal{G}^i(\mathbf{u}, \vartheta)}{\partial\vartheta}\delta\vartheta \right) \, d\Gamma, \tag{19}$$

where the displacement and crack phase field test functions are defined in accordance to the transgranular failure problem.

The finite element discretization of the weak forms given in Eqs. (17)–(19) is performed complying with the isoparametric concept. Through the definition of the Lagrangian shape functions $N^l(\boldsymbol{\xi})$, which are defined in the parametric space $\boldsymbol{\xi} = \{\xi^1, \xi^2\}$, the following discretization scheme for the displacements and the crack phase variable at the grains are introduced:

$$\mathbf{x} \cong \mathbf{N}\tilde{\mathbf{x}}; \quad \mathbf{u} \cong \mathbf{N}\mathbf{d}; \quad \delta\mathbf{u} \cong \mathbf{N}\delta\mathbf{d}; \quad \Delta\mathbf{u} \cong \mathbf{N}\Delta\mathbf{d}, \tag{20}$$

$$\mathfrak{d} \cong \mathbf{N}\bar{\mathfrak{d}}; \quad \delta\mathfrak{d} \cong \mathbf{N}\delta\bar{\mathfrak{d}}; \quad \Delta\mathfrak{d} \cong \mathbf{N}\Delta\bar{\mathfrak{d}}, \quad (21)$$

where the interpolation functions are arranged in the operator \mathbf{N} ; the nodal reference positions are collected in the vector $\bar{\mathbf{x}}$, whereas the nodal displacements and crack phase field variable are denoted by the vectors \mathbf{d} and $\bar{\mathfrak{d}}$, respectively. Moreover, the nodal trial and incremental displacements are denoted by $\delta\mathbf{d}$ and $\Delta\mathbf{d}$, respectively, whereas the corresponding vectors for the crack phase field variable are identified by $\delta\bar{\mathfrak{d}}$ and $\Delta\bar{\mathfrak{d}}$. Note that the current modeling framework adopts the same interpolation scheme for the displacement and the phase field variables, as given in Eqs. (20)–(21). In particular, with respect to the phase field interpolation, the average value of the phase field at the two flanks of the grain boundary is computed, to be associated to the midline which is taken as the usual reference in CZM formulations (see [44]). This leads to a straightforward implementation within a monolithic fully implicit solution algorithm, as herein pursued. Nevertheless, it is worth mentioning that different interpolation schemes could be exploited and easily implemented within a staggered (sequential) approach, where the phase field Poisson-type partial differential equation is solved separately from the nonlinear mechanical equilibrium problem and an overall convergence loop is introduced. Based on the authors' experience, the monolithic approach was found to be faster to converge than the staggered one, see the specific convergence study for fracture in solid shells reported in [40]. Within a monolithic strategy, coupling of different discretization schemes for the phase field and for the displacement field could be achieved by a Lagrange multiplier approach, such as the mortar method, which is a solution worth exploring in future developments.

The interpolation of the strain field ($\boldsymbol{\varepsilon}$) and the gradient of the phase field ($\nabla_{\mathbf{x}}\mathfrak{d}$), their variations ($\delta\boldsymbol{\varepsilon}$) and ($\nabla_{\mathbf{x}}\delta\mathfrak{d}$), and their increments ($\Delta\boldsymbol{\varepsilon}$) and ($\nabla_{\mathbf{x}}\Delta\mathfrak{d}$) read

$$\boldsymbol{\varepsilon} \cong \mathbf{B}_d\mathbf{d}; \quad \delta\boldsymbol{\varepsilon} \cong \mathbf{B}_d\delta\mathbf{d}; \quad \Delta\boldsymbol{\varepsilon} \cong \mathbf{B}_d\Delta\mathbf{d} \quad (22)$$

$$\nabla_{\mathbf{x}}\mathfrak{d} \cong \mathbf{B}_\mathfrak{d}\bar{\mathfrak{d}}; \quad \nabla_{\mathbf{x}}(\delta\mathfrak{d}) \cong \mathbf{B}_\mathfrak{d}\delta\bar{\mathfrak{d}}; \quad \nabla_{\mathbf{x}}(\Delta\mathfrak{d}) \cong \mathbf{B}_\mathfrak{d}\Delta\bar{\mathfrak{d}}, \quad (23)$$

where \mathbf{B}_d denotes the displacement–strain compatibility operator, and $\mathbf{B}_\mathfrak{d}$ identifies the suitable matrix for the interpolation of the gradient of the phase field variable.

After some straightforward operations, the consistent linearization of the discrete residual equations leads to the following coupled system:

$$\begin{bmatrix} \mathbf{K}'_{dd} & \mathbf{K}'_{d\mathfrak{d}} \\ \mathbf{K}'_{\mathfrak{d}d} & \mathbf{K}'_{\mathfrak{d}\mathfrak{d}} \end{bmatrix} \begin{bmatrix} \Delta\mathbf{d} \\ \Delta\mathfrak{d} \end{bmatrix} = \begin{bmatrix} \mathbf{f}'_{d,\text{ext}} \\ 0 \end{bmatrix} - \begin{bmatrix} \mathbf{f}'_{d,\text{int}} \\ \mathbf{f}'_{\mathfrak{d}} \end{bmatrix}, \quad (24)$$

where \mathbf{K}'_{ab} , with $a, b = \mathbf{d}, \mathfrak{d}$ are the tangent matrices to trigger transgranular failure within the grains, $\mathbf{f}'_{d,\text{ext}}$ is the external force vector, whereas the internal residuals corresponding to the displacements and the crack phase field variable are denoted by $\mathbf{f}'_{d,\text{int}}$ and $\mathbf{f}'_{\mathfrak{d}}$, respectively.

In an analogous manner, for the intergranular failure along the interface, the local gap vector \mathbf{g}_{loc} at any point inside Γ_i^{el} can be interpolated as follows

$$\mathbf{g}_{\text{loc}} \cong \hat{\mathbf{R}}\hat{\mathbf{B}}_b\mathbf{d} \quad (25)$$

where $\hat{\mathbf{R}}$ denotes the standard rotation matrix of the interface traction–separation relation, whilst $\hat{\mathbf{B}}_d = \mathbf{N}\mathbf{L}$ is the interface compatibility operator. For the crack phase field variables at the interface, the interpolation of the average value defined on the middle interface surface renders

$$\mathfrak{d} \cong \mathbf{N}_\mathfrak{d}\mathbf{M}_\mathfrak{d}\bar{\mathfrak{d}} = \hat{\mathbf{B}}_\mathfrak{d}\bar{\mathfrak{d}}, \quad (26)$$

where $\mathbf{M}_\mathfrak{d}$ is a suitable average operator and $\hat{\mathbf{B}}_\mathfrak{d} = \mathbf{N}_\mathfrak{d}\mathbf{M}_\mathfrak{d}$ stands for the compatibility operator corresponding to the phase field. The particular expressions of the previous interpolation operators are detailed in [56,57] and are omitted here for brevity reasons.

Finally, the discrete system of equations involving the displacement and the phase fields for intergranular failure renders

$$\begin{bmatrix} \mathbf{K}^i_{dd} & \mathbf{K}^i_{d\mathfrak{d}} \\ \mathbf{K}^i_{\mathfrak{d}d} & \mathbf{K}^i_{\mathfrak{d}\mathfrak{d}} \end{bmatrix} \begin{bmatrix} \Delta\mathbf{d} \\ \Delta\mathfrak{d} \end{bmatrix} = \begin{bmatrix} \mathbf{f}^i_d \\ \mathbf{f}^i_{\mathfrak{d}} \end{bmatrix}. \quad (27)$$

The particular expressions for tangent operators \mathbf{K}_{ab}^i , with $a, b = \mathbf{d}, \mathfrak{d}$, and for the internal force vectors \mathbf{f}_d^i and $\mathbf{f}_\mathfrak{d}^i$ are comprehensively derived in [44].

The numerical solution procedure for the systems Eqs. (24) and (27) is performed in a monolithic manner. In particular, two user-defined elements for the intergranular and transgranular failure are implemented into the FE code FEAP [58].

2.3. Anisotropic polycrystalline Silicon: grains material model

With regard to the material anisotropy, the stress–strain relation for a 3D Silicon polycrystal is usually specified in a frame with coordinate axes aligned along with its symmetry planes, i.e., using Miller’s indices, $\langle 100 \rangle$, $\langle 010 \rangle$, and $\langle 001 \rangle$.

In this material frame, the stress–strain relation can be symbolically written as $\sigma_{ij}^{\text{local}} = C_{ijkl}^{\text{local}} \varepsilon_{kl}^{\text{local}}$, where C_{ijkl}^{local} is the fourth order anisotropic constitutive tensor. For the particular case of Silicon, due to its cubic symmetry, we have $C_{1111} = C_{2222} = C_{3333} = 165.7$ GPa, $C_{1122} = C_{1133} = C_{2211} = C_{2233} = C_{3311} = C_{3322} = 63.9$ GPa, $C_{1313} = C_{3113} = C_{1331} = C_{3131} = 79.6$ GPa, $C_{2323} = C_{3223} = C_{2332} = C_{3232} = 79.6$ GPa, and $C_{1212} = C_{2112} = C_{1221} = C_{2121} = 79.6$ GPa.

To effectively account for the material properties in the general global setting, a generic orientation can be characterized by the three Euler angles defining the intersection between the surface plane $[abc]$ of the grain defined by its normal vector $\langle abc \rangle$ and the symmetry planes $[100]$, $[010]$, and $[001]$. We shall denote these angles as θ_{100} , θ_{010} , and θ_{001} , for simplicity of the notation. They can be easily computed from the Miller’s indices a, b, c , as follows:

$$\theta_{100} = \text{acos} \left(\frac{a}{\sqrt{a^2 + b^2 + c^2}} \right), \theta_{010} = \text{acos} \left(\frac{b}{\sqrt{a^2 + b^2 + c^2}} \right), \theta_{001} = \text{acos} \left(\frac{c}{\sqrt{a^2 + b^2 + c^2}} \right).$$

Thus, the stress–strain constitutive relation for each arbitrarily oriented grain in the global reference system reads $\sigma_{ij}^{\text{global}} = C_{ijkl}^{\text{global}} \varepsilon_{kl}^{\text{global}}$, where $C_{ijkl}^{\text{global}} = R_{pi} R_{qj} R_{rk} R_{sl} C_{pqrs}^{\text{local}}$ (repeated indices denote summation from 1 to 3). The rotation matrix \mathbf{R} appearing in this transformation formula can be computed as the product $\mathbf{R}_{001} \mathbf{R}_{010} \mathbf{R}_{100}$, whose terms are defined as follows:

$$\mathbf{R}_{100} = \begin{bmatrix} 1 & 0 & 0 \\ 0 & \cos(\theta_{100}) & -\sin(\theta_{100}) \\ 0 & \sin(\theta_{100}) & \cos(\theta_{100}) \end{bmatrix}, \tag{28a}$$

$$\mathbf{R}_{010} = \begin{bmatrix} \cos(\theta_{010}) & 0 & \sin(\theta_{010}) \\ 0 & 1 & 0 \\ -\sin(\theta_{010}) & 0 & \cos(\theta_{010}) \end{bmatrix}, \tag{28b}$$

$$\mathbf{R}_{001} = \begin{bmatrix} \cos(\theta_{001}) & -\sin(\theta_{001}) & 0 \\ \sin(\theta_{001}) & \cos(\theta_{001}) & 0 \\ 0 & 0 & 1 \end{bmatrix}. \tag{28c}$$

The derivation of a closed-form expression for $\mathbf{C}_{\text{global}}$ is very lengthy and impractical to display, so that it is more convenient to proceed numerically based on the above transformation.

Moreover, since the computational model of the solar cell addressed in this work complies with plane stress modeling assumptions, the determination of the 2D constitutive stress–strain tensor \mathbf{C}_{2D} of the anisotropic grain is therefore required. This can be derived by imposing that the stress components σ_{zz} , σ_{xz} , and σ_{yz} are equal to zero. From the computational point of view, it is convenient to compute the tensor $\mathbf{D} = \mathbf{C}_{\text{global}}^{-1}$ relating the strain components to the stresses as a first operation, and then to take the sub-matrix $\mathbf{D}_{3 \times 3}$ whose components $D_{3 \times 3}(i, j)$ are those contained in $D(i, j)$ with $i, j = 1, 2, 6$. The desired expression for \mathbf{C}_{2D} is finally obtained by inverting $\mathbf{D}_{3 \times 3}$, i.e., $\mathbf{C}_{2D} = \mathbf{D}_{3 \times 3}^{-1}$.

The present method for the computation of the constitutive tensors has been implemented in the MATLAB routine Cmat.m, which is provided open source as a complementary electronic material of this article.

3. Anisotropic elastic parameters and fracture toughness depending on grain orientation

The elastic properties of Silicon crystals are strongly dependent on their orientation, as carefully pointed out in [59], and their variations can be quite significant. Hence, stochastic models accounting for the random orientation of the

crystals on their anisotropic constitutive relation are relevant in practical applications. Similarly, the fracture toughness is found to be dependent on the grain orientation, see [60].

On these topics, the existing literature is quite vast, especially for polycrystalline Silicon used for microsystems [61,62,10]. In such a case, thin film Silicon is produced from epitaxial growth, and therefore the microcrystalline grains share the same growth orientation in an average sense, and only the in-plane orientation of each Silicon lattice is random. For such a material, an anisotropic elastic model is put forward for the grains and the fracture toughness is also considered dependent on the grain orientation, see [10]. For MEMS, the $\langle 110 \rangle$ orientation is associated to the lowest fracture toughness.

For solar-grade polycrystalline Silicon used to manufacture solar cells, the production process relies on laser sawing of a Silicon wafer produced by melt growth, which leads to a complete 3D random orientation of the grains [63]. From the experimental point of view, grain orientation can be measured with accuracy by X-ray diffraction (XRD) or electron back scattered diffraction (EBSD). However, these methods need a sophisticated specimen preparation and can be applied on small samples of a few micrometers only. Since the grain sizes of typical polycrystalline Silicon wafers are in the few centimeters range, the application of these methods to the analysis of solar cells composed of hundreds of centimeter-size grains is a concern.

Very recently, a new method has been proposed to enable the measurement of the grain orientations of a complete wafer [64], relying on the Laue scanner technology. Alternatively, optical microscopy imaging techniques can be applied as in [65], although a preliminary surface treatment of the wafer by an anisotropic wet chemical process is required, which excludes the applicability of this technique to solar cells embedded into photovoltaic (PV) modules.

By exploiting the effect of anisotropy on the reflectance of the grains [66], photoluminescence (PL) has also been proposed in [67] to estimate grain orientations. The analysis of PL images highlighted a strong correlation between the PL intensity and the surface energy. As a general trend, the brightest grains were found to be close to the $\langle 100 \rangle$ orientation (i.e., the visible surface plane of the grain is $[100]$), while the dimmer grains were mostly aligned along the $\langle 111 \rangle$ orientation. Grains approximately oriented along $\langle 010 \rangle$ presented an intermediate PL intensity and the widest scatter in the surface energy. Although probability density functions of the surface energy with the grain orientation were not provided, the widest scatter in the surface energy noticed for the $\langle 010 \rangle$ direction supports the hypothesis that the majority of the grain population is composed of such grains.

A closer look in [68] at the optical properties of polycrystalline Silicon using the near infrared (NIR) polariscopy and the calibration with X-ray diffraction, considering the fact that the incident light is partially absorbed, reflected and transmitted, led to the observation that the brightest grains observed during light transmission have the $\langle 344 \rangle$ orientation, the medium bright category corresponds to the $\langle 100 \rangle$ crystallographic orientation, medium dark intensities correspond to $\langle 110 \rangle$ and $\langle 211 \rangle$ orientations, and $\langle 111 \rangle$ oriented grains were found considerably darker than all the rest.

In the present study, the important observations on the correlation between light transmittance and grain orientation are further exploited to qualitative assess grain orientations in polycrystalline Silicon solar cells embedded in semi-transparent glass–glass PV modules. Such a PV laminate composition allows examining the transmitted light just by taking a photo with a CCD camera of the solar cell from its backside in illuminated sunlight conditions. After conversion of the photo into a gray scale image using the standard `rgb2grey` command in MATLAB, the image appears as that shown in Fig. 3(a).

The level of gray intensity of the transmitted light through the polycrystal, ranging from 0 for black up to 255 for white, can be examined by inspecting the corresponding histogram displaying the number of pixels with a certain gray intensity, see Fig. 3(b) related to Fig. 3(a). Although a calibration with other techniques should be made to propose a quantitative identification procedure, the considerations on the level of brightness of grains depending on their orientation gained from NIR polariscopy can be assumed to be valid also for these images, since they also refer to transmitted light. Obviously, the absolute value of the brightness of the transmitted light obtained with the NIR polariscopy in [68] for the different orientation of the Silicon grains cannot be directly compared to that obtained with a CCD camera, since they refer to a different range of the light spectrum. However, the results of the study with the NIR polariscopy can be extrapolated to interpret, in a qualitative way, the data obtained from a CCD camera. A wide inspection of the histograms of the transmitted visible light associated to more than 50 images like that in Fig. 3(a) has put into evidence some common features that can be summarized as follows (see also Fig. 3(b) for a visual representation). (i) The darkest pixels with an intensity less than that corresponding to a local minimum (75 for the histogram in Fig. 3(b)) are related to the solar cell borders, which are darker than the rest of the solar cell due to a different coating, not for a different grain orientation. Therefore, this tail of the histogram should be discarded

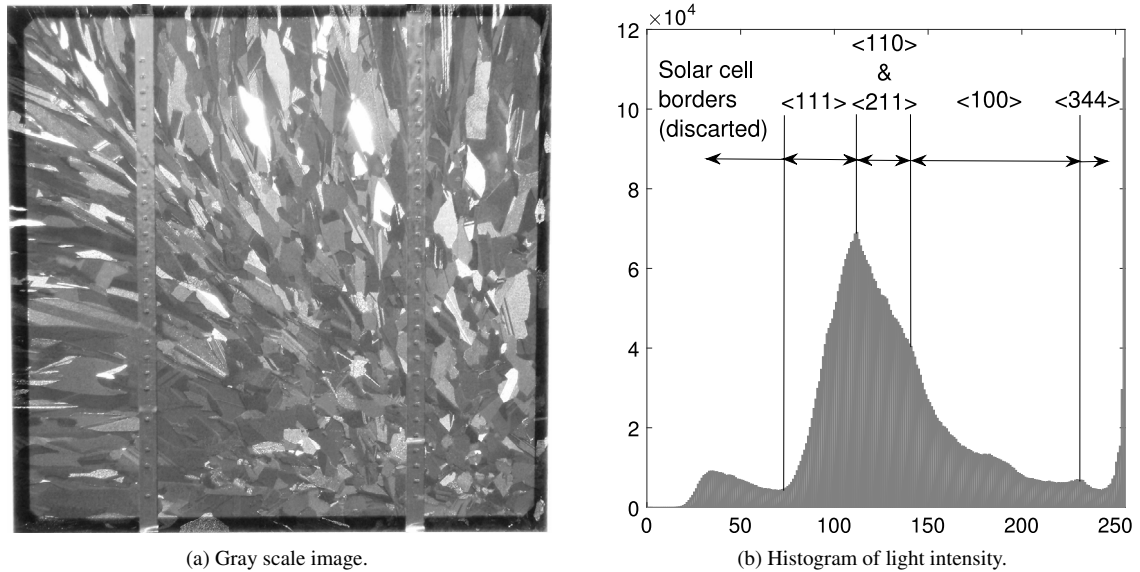


Fig. 3. (a) Gray scale image of a polycrystalline Silicon solar cell. (b) Histogram of transmitted light intensity, with the indication of the corresponding grain orientations.

since it is meaningless. (ii) The histograms present an intensity approximately in the middle of the range 0–255 that corresponds to an absolute maximum (for the value 110 in Fig. 3(b)). According to considerations based on NIR polariscopy, since the pixels associated to an intensity near this peak are medium-dark, they should be associated to $\langle 111 \rangle$, $\langle 110 \rangle$ and $\langle 211 \rangle$ grain orientations, with $\langle 111 \rangle$ grains darker than the others. Conventionally, we propose to associate $\langle 111 \rangle$ grains to intensities ranging from that corresponding to the local minimum of the histogram previously identified (75 for this example), up to the intensity corresponding to the histogram maximum. Grains with $\langle 110 \rangle$ and $\langle 211 \rangle$ orientations can be associated to intensities ranging from that of the histogram maximum, up to the intensity related to a change in the slope of the histogram (about 140 in Fig. 3(b)). The upper limit of this range is again a conventional choice, although justified by the evidence from NIR polariscopy that the $\langle 100 \rangle$ grains are 1.5 to 2 times brighter than the grains having orientations $\langle 110 \rangle$ and $\langle 211 \rangle$ [68]. (iii) The longest tail of the histogram, ranging from the intensity corresponding to the change in the slope up to the last local maximum (about 230 in Fig. 3(b)), corresponds to medium bright grains. In analogy with NIR polariscopy considerations, these medium bright grains can be considered oriented along the $\langle 100 \rangle$ direction. (iv) The last part of the histogram with intensities up to 255 corresponds to the brightest grains, and therefore they can be assumed to be oriented along the $\langle 344 \rangle$ direction.

According to this proposed classification, image segmentation of Fig. 3(a) using the above ranges of intensities leads to the images in Fig. 4, corresponding to the four major classes of grain orientations that can be ascertain from the intensity of transmitted light. These results, albeit qualitative, can be profitably used for the design of numerically generated synthetic polycrystalline microstructures of solar cells, by assigning a frequency of grains consistent with their computed densities. From Fig. 4, for instance, $\langle 111 \rangle$ grains are 26% of the total, $\langle 110 \rangle$ and $\langle 211 \rangle$ grains are 37%, $\langle 100 \rangle$ grains are 30%, and $\langle 344 \rangle$ grains are 7%. Further analysis of the shape of the grains with the same orientation (Fig. 4) could also be put forward to assess the grain size distribution and higher order geometrical parameters associated to the distortion of the grain shapes. All of this information can be used to build realistic synthetic models of grain microstructures, with different levels of accuracy depending on the need.

Considering the orientations above, which are the most frequent in polycrystalline solar cells based on the quantitative measurement techniques in [67,68], the method detailed in Section 2 is able to provide the elastic coefficients entering the 3D and the 2D plane stress anisotropic constitutive tensors for each grain orientation. These data, that cannot be easily found in the literature, are fully collected in Appendix A, along with the Euler angles corresponding to each crystallographic orientation.

As far as the fracture toughness of the grains, not all the possible grain orientations have been tested in the literature to accurately estimate the corresponding fracture toughness. Reliable data are reported in [60] for the $\langle 100 \rangle$, $\langle 110 \rangle$,

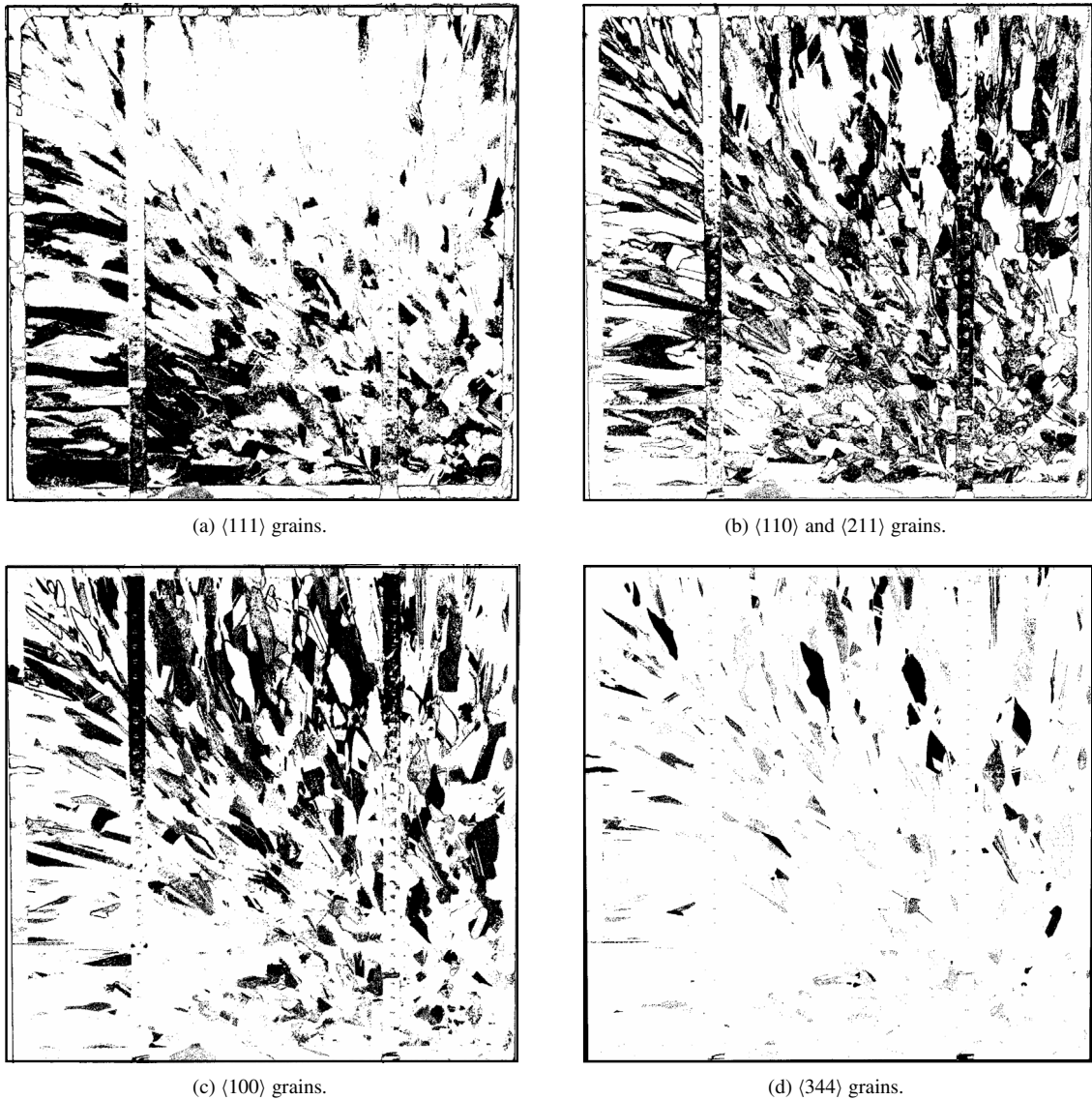


Fig. 4. Image segmentation of the gray scale image of the polycrystalline Silicon solar cell in Fig. 3(a), according to the classification in Fig. 3(b).

and $\langle 111 \rangle$ orientations, namely $\mathcal{G}^{(100)} = 4.32$ N/m, $\mathcal{G}^{(110)} = 2.96$ N/m, and $\mathcal{G}^{(111)} = 2.04$ N/m, respectively. For such a reason, we shall restrict our numerical simulations to microstructures with grains presenting those orientations.

4. Algorithm for finite element mesh discretization of polycrystalline material microstructures

This section presents an algorithm for the generation of two dimensional finite element models of solar cells with a polycrystalline microstructure, including both a procedure to discretize the grains with triangular or quadrilateral finite elements with linear shape functions, and automatically including four nodes linear interface finite elements along the grain boundaries. The algorithm has been implemented in a series of MATLAB routines (Apolygrainmicrostructure.m, C1intelementsforQ4.m, C2intelementsforT3.m) provided open access as a complementary material of this article. The procedure consists of the following three main steps:

1. The internal boundaries of the polycrystalline microstructure is generated. A user defined number of grains with random size and shape are created within a pre-defined square or rectangular domain by means of the Voronoi algorithm. The input parameters are the size of the domain, the number of grains to be generated, and the average size for the finite elements that are created in step 2.
2. Grains defined by the internal and external boundaries are meshed with two dimensional finite elements with linear shape functions. They can be either triangular or quadrangular, as specified by the user, while a mix of the two types is not possible in the present version, but it can certainly be included in further developments. The internal grain boundaries are also meshed with line elements. This will be useful in the third step of the algorithm to correctly identify the segments along which the interface elements have to be introduced. The mesh is created with the code Gmsh [69], using the output file of the step 1 in input. At this stage, all the grains are fully bonded together.
3. Interface elements are now inserted in the mesh along the grain boundaries. First, the grains are shrunk by a small amount defined by the user (1% of the original size is usually appropriate), with respect to each polygon center of mass. The nodes along the grain boundaries are duplicated. Four nodes 2D interface elements are then created along the grain boundaries using the original nodes and the duplicated ones. Two output files are finally provided: one containing the list of nodes with node number and nodal coordinates, the other containing the list of finite elements with element number and nodal connectivity data. Such files can be directly used as input for any finite element software. In the present version, the format has been particularized for being included in FEAP [58] input files.

5. Numerical examples

A square polycrystalline microstructure with 20 mm of lateral size and composed of 11 grains to resemble a portion of a real polycrystalline Silicon solar cell (see also [14]) is herein considered as a case study to assess the capability of the proposed computational framework to predict intergranular fracture, transgranular fracture, and failure modes characterized by their interplay.

The finite element mesh of the grains and of the interfaces have been generated using the algorithm thoroughly detailed in Section 4, see the result in Fig. 5. Each grain has been associated with a random orientation chosen among $\langle 100 \rangle$, $\langle 110 \rangle$, and $\langle 111 \rangle$ orientations. Based on that, each grain has its own elastic constitutive tensor and its own fracture toughness. Alternatively, to highlight the relevance of anisotropy, a model with the same geometry but with all $\langle 100 \rangle$ equi-oriented grains and the same associated toughness has been considered, which reduces to an isotropic material model.

In the simulated tensile tests, a vertical displacement v is increasingly imposed to the nodes belonging to the upper side of the specimen, keeping restrained the opposite side to vertical displacements. The corner node on the bottom left is also restrained in the horizontal direction, to avoid rigid body motion.

Due to the presence of an initial defect inside one grain (the grain displayed in red in Fig. 5), modeled as an edge crack on the left boundary, which could be for instance originated by soldering of a busbar onto the solar cell during production, the phase field approach for brittle fracture governs its initial transgranular propagation. Afterwards, when the crack meets the grain boundary, competition with cohesive intergranular fracture may occur depending on the toughness of the interface. Therefore, a series of parametric analyses, considering different values of the interface fracture toughness, has been carried out to elucidate on this competition. Finally, the same anisotropic polycrystalline microstructure has been tested again, but now without the initial defect. This example is aimed at showing the capability of the present framework to simulate not only crack growth, but also crack nucleation.

In all the simulations, the length scale parameter l of the phase field formulation for brittle fracture has been set equal to 0.002 mm to reproduce a tensile strength of 190 MPa typical of Silicon, following the identification procedure discussed in [70,71,44]. Furthermore, this particular value of the parameter l ensures the competition between the intergranular and the transgranular failure modes due to the fact that the corresponding length scales of the phase field approach l and the process zone size of the cohesive zone model, l_{CZM} , have the same order of magnitude, see [44]. Under these conditions, the interplay between both fracture phenomena can take place. In addition to these aspects, preliminary numerical simulations were conducted in order to guarantee that the mesh size has been set sufficiently fine to properly discretize the process zone of intergranular cohesive cracks and, at the same time, the damage zone induced by the phase field, thus ensuring mesh-independent force–displacement curves and

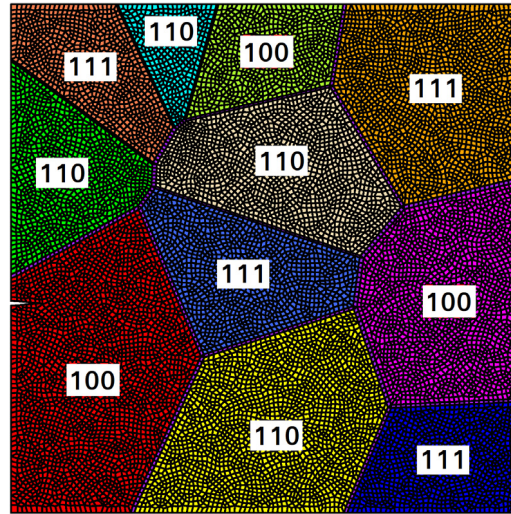


Fig. 5. Finite element mesh of the polycrystalline microstructure with quadrilateral finite elements for the continuum and compatible interface elements along the grain boundaries. An initial edge crack is inserted along the left edge, inside the red grain, to model a defect. Please refer to the online version of the article for colors. The label of each grain corresponds to its randomly assigned orientation.

crack patterns. Both conditions have been checked and satisfied by discretizing such zones where nonlinear fracture events take place with a number of finite elements ranging from 3 to 5, depending on the point. The Mode I and Mode II grain boundary fracture toughnesses are set identical, say \mathcal{G}^i , with also identical critical relative displacements in the normal and tangential directions, $g_{nc} = g_{tc} = 0.045 \mu\text{m}$. These critical relative displacements are kept constant in all the subsequent numerical tests. Therefore, different values of grain boundary toughnesses are simply the result of different peak normal and tangential cohesive tractions. It is worth noting that, in general, the intergranular fracture toughness can depend on the doping of the polycrystalline material and on the production process, so basically on the defects/inclusions introduced along the grain boundaries. Specifically, for polysilicon used for photovoltaics, experiments show that there is a mild dependence of the fracture toughness on the doping specie (Boron, Phosphorous or Antimony) [72], while a significant toughness reduction takes place only for very high Boron concentrations. The following simulations can be representative of a solar-grade polycrystalline Silicon doped with Boron or Antimony, with standard doping concentrations used in real production.

5.1. Anisotropic model with an initial defect

The fracture toughness \mathcal{G}^i of the grain boundaries is herein assumed to be proportional to the toughness of the $\langle 100 \rangle$ grains, $\mathcal{G}^{(100)}$. In the first test, the grain boundaries have been considered to be less tough than the grains, i.e., $\mathcal{G}^i / \mathcal{G}^{(100)} = 0.25$.

To visualize the crack pattern, which in the most general case is a combination of the contour where the phase field variable is equal to unity for transgranular fracture, and the portion of the grain boundaries where intergranular cracking takes place, the inelastic vertical displacement field is chosen as a representative quantity to be visualized. Such an inelastic vertical displacement field is computed as the difference between the actual vertical displacement field in the specimen and the corresponding displacement field for an intact material, which is simply a linear function of the vertical coordinate for the present uniaxial test. Therefore, the inelastic vertical displacement field is zero until localized deformation occurs. In the limit case of fracture, when the specimen is broken into two parts, the inelastic vertical displacement field is negative valued between the crack path and the constrained lower side, while it is positive valued above the crack path. Intermediate situations would occur during crack growth. The present method allows to synthetically identify the crack pattern as the curve corresponding to the transition from positive to negative inelastic displacements. Moreover, the difference between these two quantities along the crack pattern provides a measure of the vertical component of the crack opening, which is a useful quantity for fracture mechanics considerations,

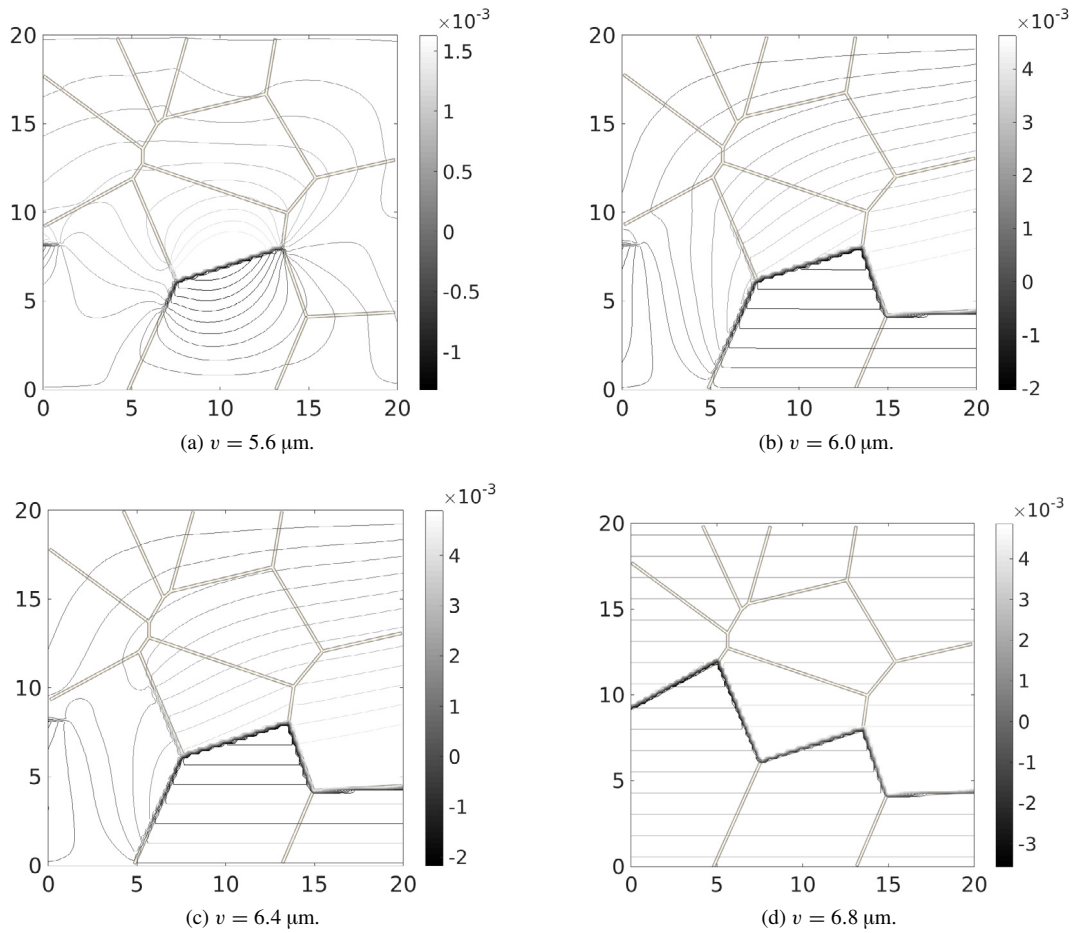


Fig. 6. Anisotropic material model. Contour lines of the inelastic vertical displacement field identifying the crack pattern, for $G^i/G^{(100)} = 0.25$.

not provided as a primary output of the phase field model of fracture. In the context of Silicon photovoltaics, for instance, the crack opening can be used as input to generalized electric models of the grid line for the assessment of power-losses of the solar cells [9,73–75].

The evolution of the inelastic vertical displacement, superimposed to the image of the grain boundaries for an easy visualization of the portions of the crack pattern involving intergranular or transgranular fracture, is shown in Fig. 6 for four different imposed vertical displacements v till complete fracture of the specimen. Such a representation with contour lines has been chosen to highlight the discontinuities in the displacement field due to the presence of cracks, which are a clear indicator for the occurrence of intergranular fracture. For $v = 5.6 \mu\text{m}$, grain boundary decohesion is competing with phase field crack growth of the initial notch. For larger imposed vertical displacements, intergranular fracture prevails and the final crack pattern is purely intergranular. A peculiarity of this specific case is a competition among intergranular crack branches: by approaching the complete failure of the specimen (Fig. 6(d)), a major intergranular crack branch appears just above the bottom left grain, whereas the down-turning branch of the crack, which propagated initially (see Figs. 6(a) and (b)) seems to disappear. Actually, the vanishing quantity in this contour plot is the crack opening and, from the mechanical point of view, this is caused by a local elastic unloading due to the appearance of the competing crack branch, which localizes the deformation in its region.

By increasing the toughness of the grain boundaries, $G^i/G^{(100)} = 0.75$, the evolution of the crack pattern illustrated in Fig. 7 shows an initial phase field crack growth of the defect within the grain where it is located, which also promotes transgranular fracture into the next adjacent grain for $v = 18.5 \mu\text{m}$. The final crack pattern at $v = 20.0 \mu\text{m}$, however,

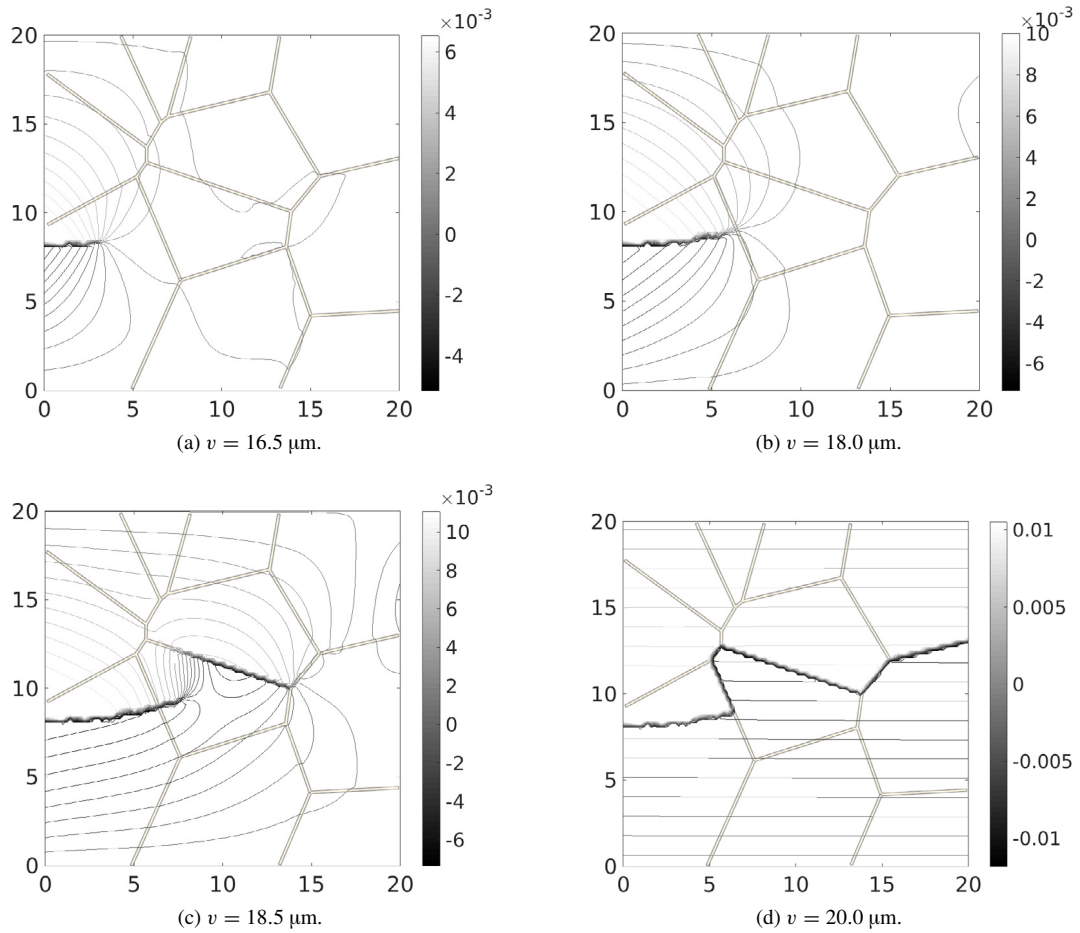


Fig. 7. Anisotropic material model. Contour lines of the inelastic vertical displacement field identifying the crack pattern, for $\mathcal{G}^i/\mathcal{G}^{(100)} = 0.75$.

is composed of an initial transgranular path followed by a sequence of intergranular paths which are localizing the deformation along the grain boundaries and are inducing a stress relief in the continuum.

A further increase of the toughness of the grain boundaries, $\mathcal{G}^i/\mathcal{G}^{(100)} = 1.00$, leads to a prevailing transgranular crack path over the whole specimen, completed by a short crack path due to intergranular crack growth for $v \geq 20.0 \mu\text{m}$, see Fig. 8.

Finally, considering grain boundaries tougher than the grains, $\mathcal{G}^i/\mathcal{G}^{(100)} = 2.00$, only transgranular crack growth is predicted to occur, see Fig. 9. Near the right hand side of the specimen, the crack path approaches the boundary between two adjacent grains, while remaining in the finite elements of the grains where the phase field variable attains unity.

The average vertical stress, σ , computed as the sum of the nodal reaction forces in the vertical direction acting on the upper side, divided by the length of the same side and the unitary out-of-plane thickness, is plotted vs. the imposed vertical displacement v and the result is shown in Fig. 10 for the different values of the toughness ratio $\mathcal{G}^i/\mathcal{G}^{(100)}$ previously considered. The case with $\mathcal{G}^i/\mathcal{G}^{(100)} = 0.25$, leading to a crack pattern at failure of pure intergranular type, is characterized by the minimum value of the peak stress. In all the other cases, the value of the peak stress is dictated by the transgranular crack growth into the first grain where the defect is located, which is a common feature for all the cases with $\mathcal{G}^i/\mathcal{G}^{(100)} \geq 0.75$. The post-peak branch of the stress–displacement curve, on the other hand, is influenced by the last part of the crack pattern, which can be intergranular or transgranular depending on the grain boundary toughness. In the case of intergranular crack growth, a more brittle post-peak branch is noticed, see the curve in Fig. 10 corresponding to $\mathcal{G}^i/\mathcal{G}^{(100)} = 0.75$.

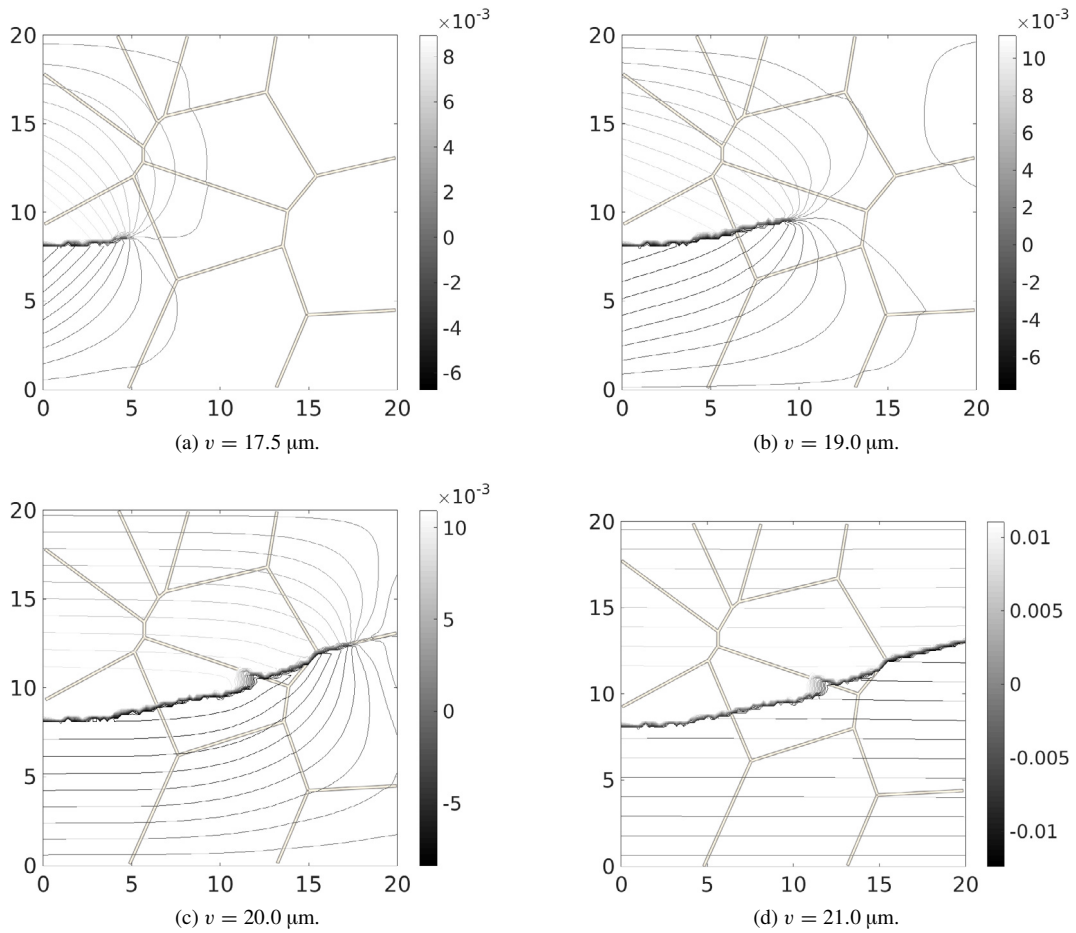


Fig. 8. Anisotropic material model. Contour lines of the inelastic vertical displacement field identifying the crack pattern, for $\mathcal{G}^i/\mathcal{G}^{(100)} = 1.00$.

5.2. Isotropic model with an initial defect

In this test, the same geometry and boundary conditions as for the anisotropic case are considered, while all the grains are assumed to be $\langle 100 \rangle$ equi-oriented, as a possible model for isotropic monocrystalline Silicon. This example encompasses a simple isotropic model, so that anisotropic effects in terms of stiffness and toughness properties are herewith precluded.

In line with the previous application, considering a grain boundary toughness $\mathcal{G}^i/\mathcal{G}^{(100)} = 2.00$, transgranular cracking is prevailing over intergranular one, as for the anisotropic case, see the crack pattern shown in Fig. 11. However, as compared to the anisotropic case, the crack path at failure is simply straight through the specimen, rather than curved as in Fig. 9. Therefore, these results pinpoint that elastic anisotropy and the dependence of the fracture toughness on the grain orientation play a decisive role on the shape of the crack path at failure.

Although the crack pattern of the isotropic material model is different from the anisotropic one, the curves relating the average vertical stress, σ , to the imposed vertical displacement, v , are similar, see Fig. 12.

5.3. Anisotropic model without defects

Finally, in this subsection, the same anisotropic model as in the test problem whose mechanical response was illustrated in Fig. 9 is examined, removing the initial defect inside the grain on the left hand side of the microstructure. Considering the high toughness of the interface as compared to that of the grains, $\mathcal{G}^i/\mathcal{G}^{(100)} = 2.00$, transgranular

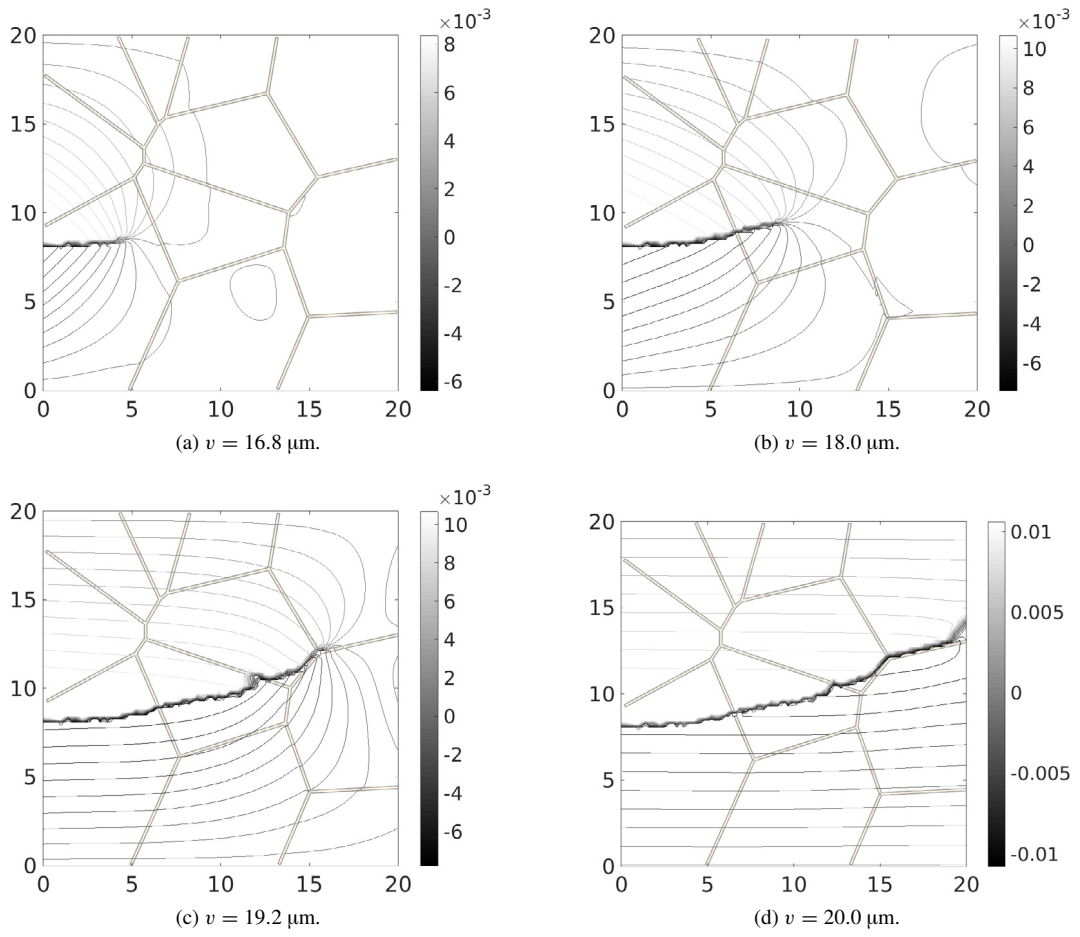


Fig. 9. Anisotropic material model. Contour lines of the inelastic vertical displacement field identifying the crack pattern, for $G^i/G^{(100)} = 2.00$.

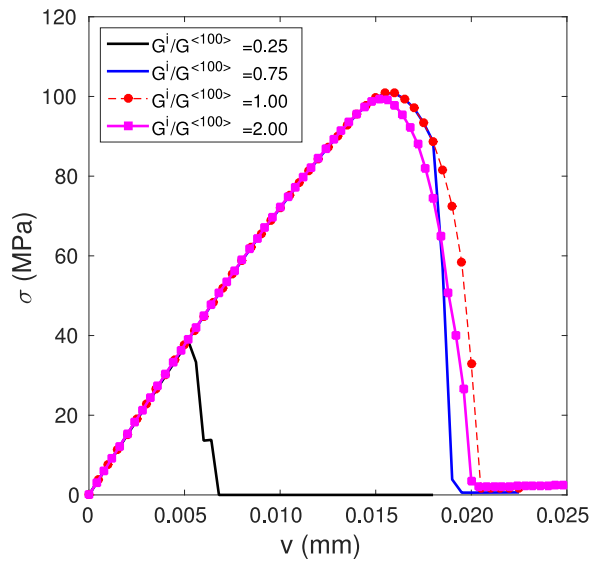


Fig. 10. Average vertical stress σ vs. imposed vertical displacement v for the anisotropic model and for different values of the toughness ratio, $G^i/G^{(100)}$.

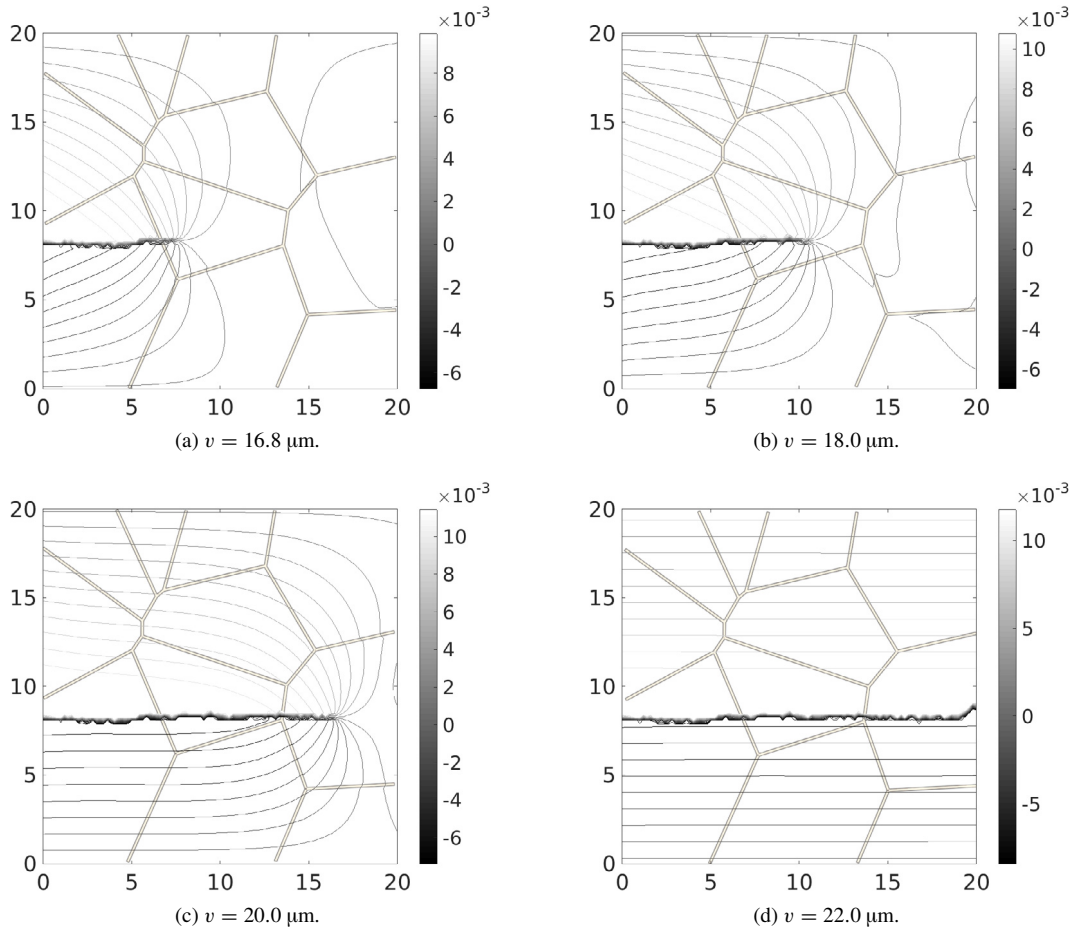


Fig. 11. Isotropic material model. Contour lines of the inelastic vertical displacement field identifying the crack pattern, for $G^i/G^{(100)} = 2.00$.

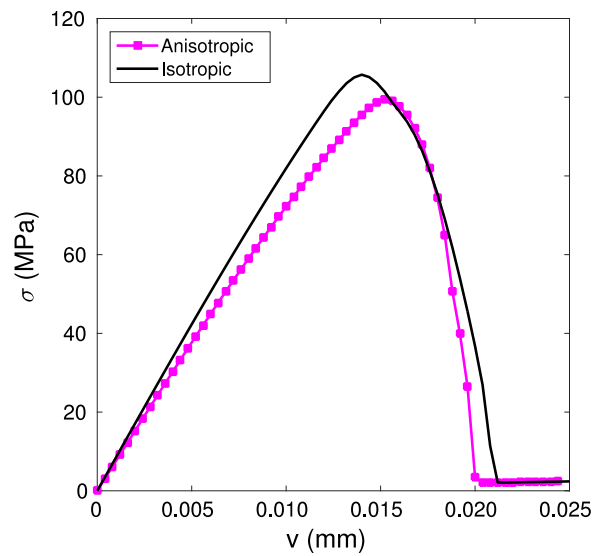


Fig. 12. Average vertical stress σ vs. imposed vertical displacement v for the isotropic and the anisotropic material models, for $G^i/G^{(100)} = 2.00$.

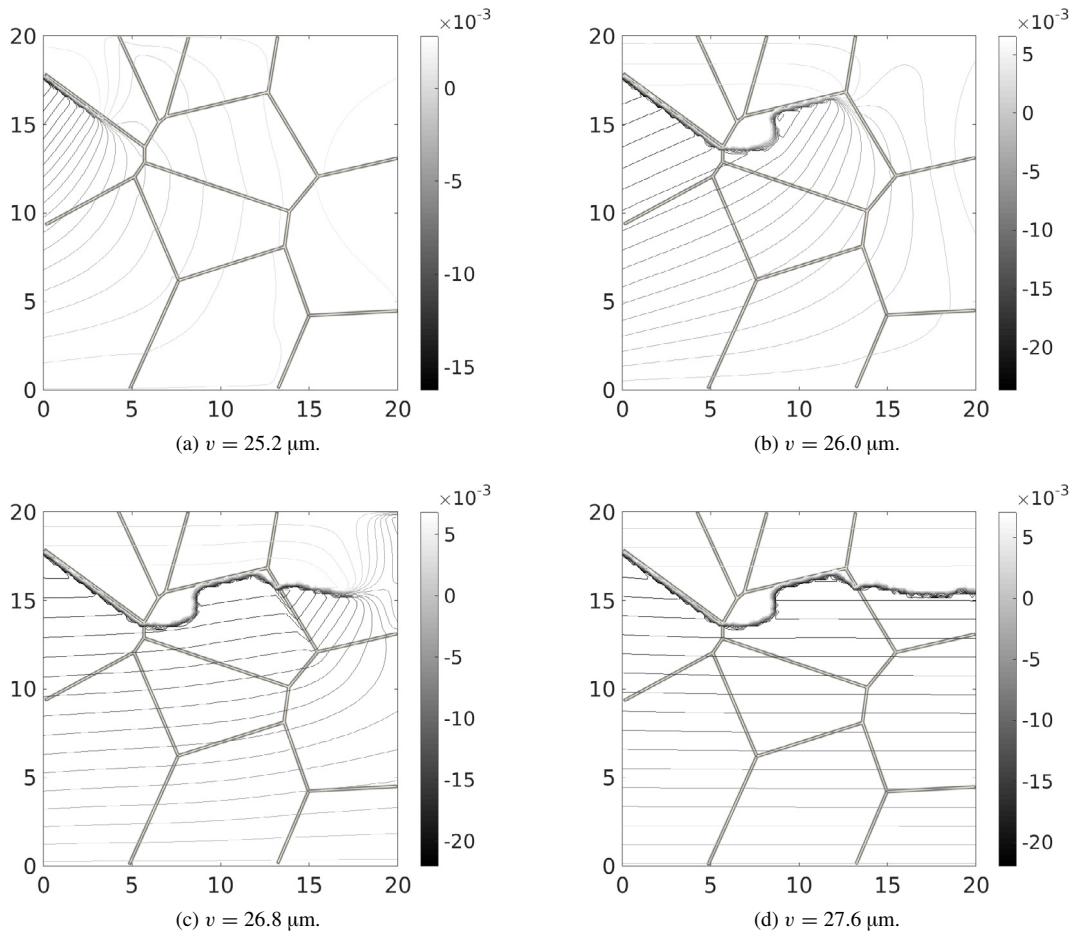


Fig. 13. Anisotropic material model without defects. Contour lines of the inelastic vertical displacement field identifying the crack pattern, for $G^i/G^{(100)} = 2.00$.

fracture is expected to prevail over the intergranular one. The evolution of the crack pattern shown in Fig. 13 confirms the trend observed in the presence of a defect, i.e., transgranular fracture only. In the absence of defects, however, the grain boundaries near the upper side of the microstructure contribute to the localization of deformation, with a phase field crack propagating very close to the material interfaces, thus leading to the occurrence of a sub-interfacial crack growth.

In terms of the overall mechanical response, see Fig. 14, the presence of an initial defect significantly reduces the value of the peak stress as compared to the un-notched case, as expected also from classical theoretical considerations. In the latter situation, the value of the peak stress significantly increases towards the nominal strength of monocrystalline Silicon, i.e., 190 MPa, but it is still lower due to strain localization effects induced by the presence of grain boundaries and material anisotropy.

6. Conclusions

In this work, a new computational framework to simulate transgranular and intergranular crack growth in anisotropic polycrystalline microstructures has been proposed. Inspired by [44], the proposed methodology enables the incorporation of the anisotropic character of solar-grade Silicon in a robust and straightforward manner. The current approach overcomes the difficulties associated with the competition between both dissipative phenomena. To do so, the interplay between the phase field approach for transgranular cracking and the cohesive zone model

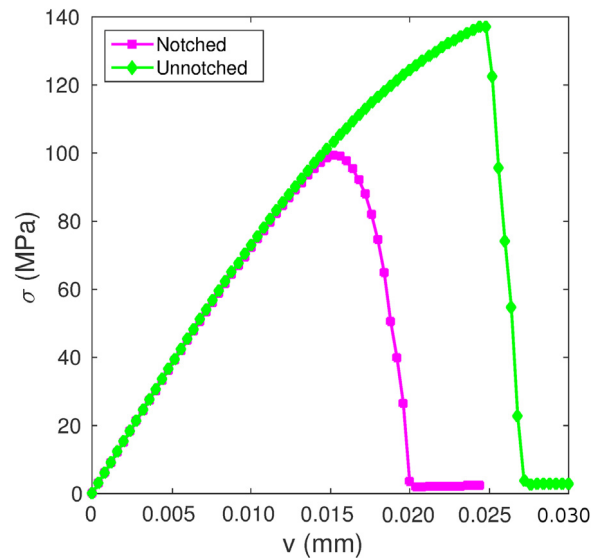


Fig. 14. Average vertical stress σ vs. imposed vertical displacement v for the anisotropic model with or without an initial defect, for $G^i/G^{(100)} = 2.00$.

for intergranular failure is carried out by stating an interface response whose stiffness depends upon the damage accumulation in the surrounding bulk. This approximation leads to a fully coupled system of equations that is solved by means of a monolithic Newton–Raphson solution scheme for the two primary fields, i.e. the displacements and the crack phase field variable.

In addition, due to its practical importance, special attention has been devoted to the identification of the anisotropic elastic parameters of the grains and the fracture toughness in solar-grade Silicon cells, which depend on grain orientation.

The proposed computational method and its predictive capabilities have been assessed by means of a series of representative tests concerning anisotropic polycrystalline Silicon microstructures. These applications show that the proposed approach is able to handle complex crack patterns and the combination of both fracture modes mentioned above. In order to draw more general conclusions, the proposed model can be applied in the future within a statistical framework, for instance Monte Carlo-based simulations, to analyze the effects of the variability of the material properties on the resulting crack pattern (as it was done, for instance, in [76] for polysilicon in MEMS). On the other hand, it is relevant to recall that recent experimental studies on full size solar-grade polycrystalline Silicon [77] have highlighted a very good reproducibility of the crack pattern in the case of twin specimens produced with exactly the same grain geometry. This evidence suggests that the scatter in the elastic and fracture properties from a specimen to another is almost negligible and that only the grain-size distribution plays a key role. Besides a statistical study, also the size of the microstructural model should be object of further studies, since the apparent strength and the crack pattern are indeed affected by the ratio between the process zone size of the intergranular cohesive cracks and the specimen size, as shown in previous studies on intergranular fracture of polycrystals [1,4].

Acknowledgments

The research presented in this article has received funding from the European Research Council through the ERC Starting Grant “Multi-field and multi-scale Computational Approach to Design and Durability of PhotoVoltaic Modules”—CA2PVM, under the European Union’s Seventh Framework Programme (FP/2007–2013)/ERC Grant Agreement no. 306622. JR is also grateful to the support to the projects funded by the Spanish Ministry of Economy and Competitiveness (Projects MAT2015–71036-P and MAT2015–71309-P) and the Andalusian Government (Projects of Excellence No. TEP-7093 and P12-TEP-1050).

Appendix A. Anisotropic elastic coefficients of the grains

This Appendix collects the 3D and 2D plane stress anisotropic elastic coefficients of the grains with the most common orientations observed in solar cells. These coefficients have been computed following the procedure presented in Section 3, by preliminary evaluating the three Euler angles for each orientation using the MATLAB script provided as additional electronic material. The unit of measure of all the coefficients is GPa.

For Silicon grains whose surface is aligned along the [100] plane ($\langle 100 \rangle$ normal vector), the three Euler angles formed with the [100], [010], and [001] planes are $\theta_{100} = 0^\circ$, $\theta_{010} = 90^\circ$, and $\theta_{001} = 90^\circ$, respectively. As a result, the 3D anisotropic constitutive tensor reads:

$$\mathbf{C}^{100} = \begin{bmatrix} 165.7 & 63.9 & 63.9 & 0 & 0 & 0 \\ 63.9 & 165.7 & 63.9 & 0 & 0 & 0 \\ 63.9 & 63.9 & 165.7 & 0 & 0 & 0 \\ 0 & 0 & 0 & 79.6 & 0 & 0 \\ 0 & 0 & 0 & 0 & 79.6 & 0 \\ 0 & 0 & 0 & 0 & 0 & 79.6 \end{bmatrix} \quad (\text{A.1})$$

and its plane stress counterpart is:

$$\mathbf{C}_{2D}^{100} = \begin{bmatrix} 141.1 & 39.3 & 0.0 \\ 39.3 & 141.1 & 0.0 \\ 0.0 & 0.0 & 79.6 \end{bmatrix}. \quad (\text{A.2})$$

For Silicon grains whose surface is aligned along the [110] plane ($\langle 110 \rangle$ normal vector), the three Euler angles are $\theta_{100} = 45^\circ$, $\theta_{010} = 45^\circ$, and $\theta_{001} = 90^\circ$. The 3D anisotropic constitutive tensor reads:

$$\mathbf{C}^{110} = \begin{bmatrix} 194.4 & 49.5 & 49.5 & -14.3 & 0 & 0 \\ 49.5 & 201.5 & 42.4 & 7.2 & 0 & 0 \\ 49.5 & 42.4 & 201.6 & 7.2 & 0 & 0 \\ -14.3 & 7.2 & 7.2 & 58.1 & 0 & 0 \\ 0 & 0 & 0 & 0 & 65.2 & -14.3 \\ 0 & 0 & 0 & 0 & -14.3 & 65.2 \end{bmatrix} \quad (\text{A.3})$$

and the plane stress tensor is:

$$\mathbf{C}_{2D}^{110} = \begin{bmatrix} 177.7 & 40.7 & 0 \\ 40.7 & 192.1 & 0 \\ 0 & 0 & 62.1 \end{bmatrix}. \quad (\text{A.4})$$

For Silicon grains whose surface is aligned along the [111] plane ($\langle 111 \rangle$ normal vector), the three Euler angles are $\theta_{100} = \theta_{010} = \theta_{001} = 54.7^\circ$. The 3D anisotropic constitutive tensor reads:

$$\mathbf{C}^{111} = \begin{bmatrix} 194.1 & 45.5 & 53.9 & -4.5 & 8.9 & 9.6 \\ 45.5 & 186.2 & 61.8 & 1.4 & 5.1 & -13.4 \\ 53.9 & 61.8 & 177.8 & 3.1 & -14.1 & 3.7 \\ -4.5 & 1.4 & 3.1 & 77.5 & 3.7 & 5.1 \\ 8.9 & 5.1 & -14.1 & 3.7 & 69.6 & -4.5 \\ 9.6 & -13.4 & 3.7 & 5.1 & -4.5 & 61.2 \end{bmatrix} \quad (\text{A.5})$$

and the plane stress tensor is:

$$\mathbf{C}_{2D}^{111} = \begin{bmatrix} 174.6 & 24.8 & 9.7 \\ 24.8 & 163.3 & -14.0 \\ 9.7 & -14.0 & 60.5 \end{bmatrix}. \quad (\text{A.6})$$

Table A.1

Eigenvalues of the constitutive tensor and Young’s modulus, E , depending on the grain orientation.

Grain orientation	λ_1 (GPa)	λ_2 (GPa)	λ_3 (GPa)	E (GPa)
(100)	180.3	101.8	79.6	130.1
(110)	226.3	143.6	62.1	169.1
(111)	194.4	146.8	57.1	187.8
(211)	214.2	130.4	66.8	169.1
(344)	198.9	150.2	56.3	185.4

For Silicon grains whose surface is aligned along the [211] plane ((211) normal vector), the three Euler angles are $\theta_{100} = 35.26^\circ$, $\theta_{010} = 65.90^\circ$, and $\theta_{001} = 65.90^\circ$. The 3D anisotropic constitutive tensor reads:

$$\mathbf{C}^{211} = \begin{bmatrix} 182.1 & 55.5 & 55.9 & -5.9 & 13.0 & 8.0 \\ 55.5 & 193.1 & 44.9 & -6.9 & -7.6 & -9.4 \\ 55.9 & 44.8 & 192.7 & 12.9 & -5.4 & 1.4 \\ -5.9 & -6.9 & 12.9 & 60.6 & 1.4 & -7.6 \\ 13.0 & -7.6 & -5.4 & 1.4 & 71.6 & -5.9 \\ 8.0 & -9.4 & 1.4 & -7.6 & -5.9 & 71.2 \end{bmatrix} \tag{A.7}$$

and the plane stress tensor is:

$$\mathbf{C}_{2D}^{211} = \begin{bmatrix} 161.2 & 42.1 & 7.5 \\ 42.1 & 180.5 & -11.5 \\ 7.5 & -11.5 & 69.8 \end{bmatrix}. \tag{A.8}$$

For Silicon grains whose surface is aligned along the [344] plane ((344) normal vector), the three Euler angles are $\theta_{100} = 62.06^\circ$, $\theta_{010} = 51.34^\circ$, and $\theta_{001} = 51.34^\circ$. The 3D anisotropic constitutive tensor reads:

$$\mathbf{C}^{344} = \begin{bmatrix} 197.2 & 43.8 & 52.6 & -3.1 & 6.6 & 9.3 \\ 43.8 & 190.3 & 59.4 & 5.9 & 9.1 & -8.6 \\ 52.6 & 59.4 & 181.5 & -2.8 & -15.7 & -0.8 \\ -3.1 & 5.9 & -2.8 & 75.1 & -0.8 & 9.1 \\ 6.6 & 9.1 & -15.7 & -0.8 & 68.3 & -3.1 \\ 9.3 & -8.6 & -0.8 & 9.1 & -3.1 & 59.5 \end{bmatrix} \tag{A.9}$$

and the plane stress tensor is:

$$\mathbf{C}_{2D}^{344} = \begin{bmatrix} 180.0 & 24.4 & 10.3 \\ 24.4 & 167.2 & -8.5 \\ 10.3 & -8.5 & 58.2 \end{bmatrix}. \tag{A.10}$$

To appreciate the mismatch in the elastic constitutive properties, the eigenvalues of the above constitutive tensors are collected in Table A.1, together with the corresponding Young’s modulus. In particular, the Young’s moduli for the different orientations of the surface of the polycrystalline grains, defined by the normal vector $\langle abc \rangle$, have been computed from the coefficients of the compliance tensor \mathbf{D}^{100} , by applying the following equation [78]:

$$\frac{1}{E_{abc}} = D_{11} - 2 \left(D_{11} - D_{12} - \frac{1}{2} D_{66} \right) (\cos(\theta_{100})^2 \cos(\theta_{010})^2 + \cos(\theta_{010})^2 \cos(\theta_{001})^2 + \cos(\theta_{100})^2 \cos(\theta_{001})^2) \tag{A.11}$$

where $\cos(\theta_{100})$, $\cos(\theta_{010})$ and $\cos(\theta_{001})$ are the direction cosines as defined in Section 2.3.

Appendix B. Supplementary data

Supplementary electronic material related to this article can be found online at <http://dx.doi.org/10.1016/j.cma.2017.10.021>.

References

- [1] M. Paggi, P. Wriggers, A nonlocal cohesive zone model for finite thickness interfaces–Part I: mathematical formulation and validation with molecular dynamics, *Comput. Mater. Sci.* 50 (5) (2011) 1625–1633.
- [2] M. Paggi, P. Wriggers, A nonlocal cohesive zone model for finite thickness interfaces–Part II: FE implementation and application to polycrystalline materials, *Comput. Mater. Sci.* 50 (5) (2011) 1634–1643.
- [3] M. Paggi, E. Lehmann, C. Weber, A. Carpinteri, P. Wriggers, M. Schaper, A numerical investigation of the interplay between cohesive cracking and plasticity in polycrystalline materials, *Comput. Mater. Sci.* 77 (2013) 81–92.
- [4] M. Paggi, P. Wriggers, Stiffness and strength of hierarchical polycrystalline materials with imperfect interfaces, *J. Mech. Phys. Solids* 60 (4) (2012) 557–572.
- [5] H.D. Espinosa, P.D. Zavattieri, A grain level model for the study of failure initiation and evolution in polycrystalline brittle materials. Part II: Numerical examples, *Mech. Mater.* 35 (3–6) (2003) 365–394.
- [6] M. Ortiz, A. Pandolfi, Finite deformation irreversible cohesive elements for three-dimensional crack-propagation analysis, *Internat. J. Numer. Methods Engrg.* 44 (1999) 1267–1282.
- [7] T. Luther, C. Könke, Polycrystal models for the analysis of intergranular crack growth in metallic materials, *Eng. Fract. Mech.* 76 (15) (2009) 2332–2343.
- [8] C.V. Verhoosel, M.A. Gutiérrez, Modelling inter- and transgranular fracture in piezoelectric polycrystals, *Eng. Fract. Mech.* 76 (6) (2009) 742–760.
- [9] M. Paggi, M. Corrado, M.A. Rodríguez, A multi-physics and multi-scale numerical approach to microcracking and power-loss in photovoltaic modules, *Compos. Struct.* 95 (2013) 630–638.
- [10] A. Corigliano, A. Ghisi, G. Langfelder, A. Longoni, F. Zaraga, A. Merassi, A microsystem for the fracture characterization of polysilicon at the micro-scale, *Eur. J. Mech. A Solids* 30 (2) (2011) 127–136.
- [11] R. Vayrette, M. Galceran, M. Coulombier, S. Godet, J.-P. Raskin, T. Pardoën, Size dependent fracture strength and cracking mechanisms in freestanding polycrystalline silicon films with nanoscale thickness, *Eng. Fract. Mech.* 168 (Part A) (2016) 190–203.
- [12] M. Sander, S. Dietrich, M. Pander, M. Ebert, J. Bagdahn, Systematic investigation of cracks in encapsulated solar cells after mechanical loading, *Sol. Energy Mater. Sol. Cells* 111 (2013) 82–89.
- [13] L. Zhao, A. Maynadier, D. Nelias, Stiffness and fracture analysis of photovoltaic grade silicon plates, *Int. J. Solids Struct.* 97–98 (2016) 355–369.
- [14] A. Infuso, M. Corrado, M. Paggi, Image analysis of polycrystalline solar cells and modelling of intergranular and transgranular cracking, *J. Eur. Ceram. Soc.* 34 (11) (2014) 2713–2722.
- [15] M. Corrado, J.-F. Molinari, Effects of residual stresses on the tensile fatigue behavior of concrete, *Cem. Concr. Res.* 89 (2016) 206–219.
- [16] N. Moës, J. Dolbow, T. Belytschko, A finite element method for crack growth without remeshing, *Internat. J. Numer. Methods Engrg.* 46 (1) (1999) 131–150.
- [17] N. Sukumar, D.J. Srolovitz, T.J. Baker, J.-H. Prévost, Brittle fracture in polycrystalline microstructures with the extended finite element method, *Internat. J. Numer. Methods Engrg.* 56 (14) (2003) 2015–2037.
- [18] J. Oliver, A.E. Huespe, S. Blanco, D.L. Linero, Stability and robustness issues in numerical modeling of material failure with the strong discontinuity approach, *Comput. Methods Appl. Mech. Engrg.* 195 (52) (2006) 7093–7114.
- [19] C. Linder, F. Armero, Finite elements with embedded strong discontinuities for the modeling of failure in solids, *Internat. J. Numer. Methods Engrg.* 72 (12) (2007) 1391–1433.
- [20] J.C. Simo, J. Oliver, F. Armero, An analysis of strong discontinuities induced by strain-softening in rate-independent inelastic solids, *Comput. Mech.* 12 (5) (1993) 277–296.
- [21] A. Simone, C.A. Duarte, E. Van der Giessen, A generalized finite element method for polycrystals with discontinuous grain boundaries, *Internat. J. Numer. Methods Engrg.* 67 (8) (2006) 1122–1145.
- [22] C. Miehe, M. Hofacker, F. Welschinger, A phase field model for rate-independent crack propagation: Robust algorithmic implementation based on operator splits, *Comput. Methods Appl. Mech. Engrg.* 199 (45) (2010) 2765–2778.
- [23] M.J. Borden, C.V. Verhoosel, M.A. Scott, T.J.R. Hughes, C.M. Landis, A phase-field description of dynamic brittle fracture, *Comput. Methods Appl. Mech. Engrg.* 217 (2012) 77–95.
- [24] A.A. Griffith, The phenomena of rupture and flow in solids, *Phil. Trans. R. Soc. Lond. Ser. A, Contain. Pap. Math. Phys. Character* 221 (1921) 163–198.
- [25] L. Ambrosio, V.M. Tortorelli, Approximation of functional depending on jumps by elliptic functional via Γ -convergence, *Comm. Pure Appl. Math.* 43 (8) (1990) 999–1036.
- [26] G.A. Francfort, J.-J. Marigo, Revisiting brittle fracture as an energy minimization problem, *J. Mech. Phys. Solids* 46 (8) (1998) 1319–1342.
- [27] M. Frémond, B. Nedjar, Damage, gradient of damage and principle of virtual power, *Int. J. Solids Struct.* 33 (8) (1996) 1083–1103.
- [28] R.H.J. Peerlings, M.G.D. Geers, R. De Borst, W.A.M. Brekelmans, A critical comparison of nonlocal and gradient-enhanced softening continua, *Internat. J. Solids Struct.* 38 (44) (2001) 7723–7746.
- [29] C. Comi, U. Perego, Fracture energy based bi-dissipative damage model for concrete, *Int. J. Solids Struct.* 38 (36) (2001) 6427–6454.
- [30] B.J. Dimitrijevic, K. Hackl, A regularization framework for damage–plasticity models via gradient enhancement of the free energy, *Int. J. Numer. Methods Biomed. Eng.* 27 (8) (2011) 1199–1210.
- [31] C. Miehe, F. Welschinger, M. Hofacker, Thermodynamically consistent phase-field models of fracture: Variational principles and multi-field FE implementations, *Internat. J. Numer. Methods Engrg.* 83 (10) (2010) 1273–1311.
- [32] M. Hofacker, C. Miehe, A phase field model of dynamic fracture: Robust field updates for the analysis of complex crack patterns, *Internat. J. Numer. Methods Engrg.* 93 (3) (2013) 276–301.

- [33] M. Ambati, T. Gerasimov, L. De Lorenzis, Phase-field modeling of ductile fracture, *Comput. Mech.* 55 (5) (2015) 1017–1040.
- [34] O. Gültekin, Hgf. Dal, G.A. Holzapfel, A phase-field approach to model fracture of arterial walls: Theory and finite element analysis, *Comput. Methods Appl. Mech. Engrg.* 312 (2016) 542–566 Phase Field Approaches to Fracture.
- [35] C. Miehe, L.M. Schänzel, H. Ulmer, Phase field modeling of fracture in multi-physics problems. Part I. Balance of crack surface and failure criteria for brittle crack propagation in thermo-elastic solids, *Comput. Methods Appl. Mech. Engrg.* 294 (2015) 449–485.
- [36] X. Zhang, A. Krischok, C. Linder, A variational framework to model diffusion induced large plastic deformation and phase field fracture during initial two-phase lithiation of silicon electrodes, *Comput. Methods Appl. Mech. Engrg.* 312 (2016) 51–77.
- [37] F. Amiri, D. Millán, Y. Shen, T. Rabczuk, M. Arroyo, Phase-field modeling of fracture in linear thin shells, *Theor. Appl. Fract. Mech.* 69 (2014) 102–109.
- [38] P. Areias, T. Rabczuk, M.A. Msekh, Phase-field analysis of finite-strain plates and shells including element subdivision, *Comput. Methods Appl. Mech. Engrg.* 312 (2016) 322–350.
- [39] J. Kiendl, M. Ambati, L. De Lorenzis, H. Gomez, A. Reali, Phase-field description of brittle fracture in plates and shells, *Comput. Methods Appl. Mech. Engrg.* 312 (2016) 374–394.
- [40] J. Reinoso, M. Paggi, C. Linder, Phase field modeling of brittle fracture for enhanced assumed strain shells at large deformations: formulation and finite element implementation, *Comput. Mech.* 59 (2017) 981–1001.
- [41] J.D. Clayton, J. Knap, Phase field modeling of directional fracture in anisotropic polycrystals, *Comput. Mater. Sci.* 98 (2015) 158–169.
- [42] J.D. Clayton, J. Knap, Phase field modeling and simulation of coupled fracture and twinning in single crystals and polycrystals, *Comput. Methods Appl. Mech. Engrg.* 312 (2016) 447–467 Phase Field Approaches to Fracture.
- [43] T.-T. Nguyen, J. Réthoré, J. Yvonnet, M.-C. Baietto, Multi-phase-field modeling of anisotropic crack propagation for polycrystalline materials, *Comput. Mech.* (2017) 1–26.
- [44] M. Paggi, J. Reinoso, Revisiting the problem of a crack impinging on an interface: A modeling framework for the interaction between the phase field approach for brittle fracture and the interface cohesive zone model, *Comput. Methods Appl. Mech. Engrg.* 321 (2017) 145–172.
- [45] P.R. Budarapu, J. Reinoso, M. Paggi, Concurrently coupled solid shell-based adaptive multiscale method for fracture, *Comput. Methods Appl. Mech. Engrg.* 319 (2017) 338–365.
- [46] Y. Umemo, A. Kushima, T. Kitamura, P. Gumbsch, Ab initio study of the surface properties and ideal strength of (100) silicon thin films, *Phys. Rev. B* 72 (2005) 165431.
- [47] A. Saporita, M. Paggi, A coupled cohesive zone model for transient analysis of thermoelastic interface debonding, *Comput. Mech.* 53 (2014) 845–857.
- [48] J.-W. Lee, S.-H. Bae, N. De Marco, Y.-T. Hsieh, Z. Dai, Y. Yang, The role of grain boundaries in perovskite solar cells, *Mater. Today Energy*, (in press).
- [49] C.V. Verhoosel, R. de Borst, A phase-field model for cohesive fracture, *Internat. J. Numer. Methods Engrg.* 96 (1) (2013) 43–62.
- [50] H. Amor, J.-J. Marigo, C. Maurini, Regularized formulation of the variational brittle fracture with unilateral contact: numerical experiments, *J. Mech. Phys. Solids* 57 (8) (2009) 1209–1229.
- [51] E. Tanné, T. Li, B. Bourdin, J.-J. Marigo, C. Maurini, Crack nucleation in variational phase-field models of brittle fracture, *J. Mech. Phys. Solids* 110 (2017) 80–99.
- [52] C. Comi, U. Perego, Criteria for mesh refinement in nonlocal damage finite element analyses, *Eur. J. Mech. A Solids* 23 (4) (2004) 615–632.
- [53] C. Comi, S. Mariani, U. Perego, An extended FE strategy for transition from continuum damage to mode I cohesive crack propagation, *Int. J. Numer. Anal. Methods Geomech.* 31 (2007) 213–238.
- [54] B. Bourdin, G.A. Francfort, J.-J. Marigo, The variational approach to fracture, *J. Elasticity* 91 (1) (2008) 5–148.
- [55] M.-A. Msekh, J.-M. Sargado, M. Jamshidian, P.M. Areias, T. Rabczuk, Abaqus implementation of phase-field model for brittle fracture, *Comput. Mater. Sci.* 96 (2015) 472–484.
- [56] J. Reinoso, M. Paggi, A consistent interface element formulation for geometrical and material nonlinearities, *Comput. Mech.* 54 (6) (2014) 1569–1581.
- [57] M. Paggi, J. Reinoso, An anisotropic large displacement cohesive zone model for fibrillar and crazing interfaces, *Int. J. Solids Struct.* 69 (2015) 106–120.
- [58] O.C. Zienkiewicz, R.L. Taylor, *The Finite Element Method: Solid Mechanics*, Vol. 2, Butterworth-Heinemann, 2000.
- [59] M.A. Hopcroft, W.D. Nix, T.W. Kenny, What is the Young’s modulus of Silicon? *IEEE J. Micromechanical Syst.* 19 (2010) 229–238.
- [60] A. Masolin, P.O. Bouchard, R. Martini, M. Bernacki, Thermo-mechanical and fracture properties in single-crystal silicon, *J. Mater. Sci.* 48 (3) (2013) 979–988.
- [61] A. Ghisi, F. Fachin, S. Mariani, S. Zerbini, Multi-scale analysis of polysilicon MEMS sensors subject to accidental drops: Effect of packaging, *Microelectron. Reliab.* 49 (3) (2009) 340–349.
- [62] A. Ghisi, S. Kalicinski, S. Mariani, I. De Wolf, A. Corigliano, Polysilicon MEMS accelerometers exposed to shocks: numerical-experimental investigation, *J. Micromech. Microeng.* 19 (3) (2009) 035023.
- [63] K. Fujiwara, Crystal growth behaviors of Silicon during melt growth processes, *Int. J. Photoenergy* (2012) 169829.
- [64] T. Lehmann, M. Trempa, E. Meissner, M. Zschorsch, M. Reimann, J. Friedrich, Laue scanner: A new method for determination of grain orientations and grain boundary types of multicrystalline silicon on a full wafer scale, *Acta Mater.* 69 (2014) 1–8.
- [65] D. Lausch, M. Glaeser, C. Hagendorf, Determination of crystal grain orientations by optical microscopy at textured surfaces, *J. Phys. D: Appl. Phys.* 114 (2013) 194509.
- [66] B. Soporì, D. Guhabiswas, P. Rupnowski, S. Shet, S. Devayajanam, H. Moutinho, A new method for rapid measurement of orientations and sizes of grains in multicrystalline silicon wafers, in: 37th IEEE Photovoltaic Specialists Conference, June 2011, pp. 001680–001685.

- [67] H.C. Sio, Z. Xiong, T. Trupke, D. Macdonald, Imaging crystal orientations in multicrystalline silicon wafers via photoluminescence, *Appl. Phys. Lett.* 101 (8) (2012) 082102.
- [68] K. Skenes, G. Prasath, S. Danyluk, Silicon grain crystallographic orientation measurement from NIR transmission and reflection, in: 2013 IEEE 39th Photovoltaic Specialists Conference (PVSC), June 2013, pp. 0519–0522.
- [69] C. Geuzaine, J.-F. Remacle, Gmsh: A 3-D finite element mesh generator with built-in pre- and post-processing facilities, *Internat. J. Numer. Methods Engrg.* 79 (11) (2009) 1309–1331.
- [70] T.-T. Nguyen, J. Yvonnet, Q.-Z. Zhu, M. Bornert, C. Chateau, A phase-field method for computational modeling of interfacial damage interacting with crack propagation in realistic microstructures obtained by microtomography, *Comput. Methods Appl. Mech. Engrg.* 312 (2016) 567–595.
- [71] T.-T. Nguyen, J. Yvonnet, M. Bornert, C. Chateau, Initiation and propagation of complex 3D networks of cracks in heterogeneous quasi-brittle materials: direct comparison between in situ testing-microct experiments and phase field simulations, *J. Mech. Phys. Solids* 95 (2016) 320–350.
- [72] J.G. Swadener, M. Nastasi, Effect of dopants on the fracture toughness of silicon, *J. Mater. Sci. Lett.* 21 (2002) 1363–1365.
- [73] M. Paggi, I. Berardone, A. Infuso, M. Corrado, Fatigue degradation and electric recovery in Silicon solar cells embedded in photovoltaic modules, *Sci. Rep.* 4 (2014) 04506.
- [74] I. Berardone, M. Corrado, M. Paggi, A generalized electric model for mono and polycrystalline silicon in the presence of cracks and random defects, *Energy Procedia* 55 (2014) 22–29.
- [75] M. Paggi, M. Corrado, I. Berardone, A global/local approach for the prediction of the electric response of cracked solar cells in photovoltaic modules under the action of mechanical loads, *Eng. Fract. Mech.* 168 (Part B) (2016) 40–57.
- [76] S. Mariani, R. Martini, A. Ghisi, A. Corigliano, B. Simoni, Monte Carlo simulation of micro-cracking in polysilicon MEMS exposed to shocks, *Int. J. Fract.* 167 (2011) 83–101.
- [77] L. Zhao, D. Nelias, D. Bardel, A. Maynadier, P. Chaudet, B. Marie, On the fracture of multi-crystalline silicon wafer, *J. Phys. D: Appl. Phys.* 49 (2016) 475601.
- [78] L. Zhang, R. Barrett, P. Cloetens, C. Detlefs, M. Sanchez del Rio, Anisotropic elasticity of silicon and its application to the modelling of X-ray optics, *J. Synchrotron Radiat.* 21 (2014) 507–517.